AIAA Journal
Vol. 45, No. 10, October 2007

Advanced Eddy-Viscosity and Reynolds-Stress Turbulence Model Simulations of Aerospace Applications

Enda Dimitri Vieira Bigarella[*]
Instituto Tecnológico de Aeronáutica, São José dos Campos, Brazil
and
João Luiz F. Azevedo[†]
Instituto de Aeronáutica e Espaço, São José dos Campos, Brazil

DOI: 10.2514/1.29332

Recent improvements on a three-dimensional unstructured-mesh finite-volume method, which solves the Reynolds-averaged Navier–Stokes equations for complex aerospace applications, are presented. The correct modeling of turbulence effects in aerospace flows is paramount for their successful computation. Linear one- and two-equation models are considered. The linear approximation is also extended to include a nonlinear formulation resulting from an explicit algebraic Reynolds-stress model. Two Reynolds-stress closures are also available. Nonlinear eddy-viscosity and Reynolds-stress models naturally offer the potential for more reliable predictions than linear approximations because anisotropy of the Reynolds stresses can be accounted for. Experimental and direct numerical simulation results are used for verification and validation of the turbulence model implementation. Focus is directed toward the effect of anisotropy for the resolution of the interaction between shock waves and boundary layers. In general, good agreement with theoretical or experimental results is obtained.

Nomenclature

C_d = 2-D drag coefficient
C_l = 2-D lift coefficient
Cp = pressure coefficient
c_f = local skin friction coefficient
e = total energy per unit of volume
e_i = internal energy
$\hat{\imath} = \{\hat{\imath}_x, \hat{\imath}_y, \hat{\imath}_z\}$ = Cartesian unit vector
k = turbulent kinetic energy
M = Mach number
$\boldsymbol{P}_e$ = inviscid flux vector
$\boldsymbol{P}_v$ = viscous flux vector
Pr = Prandtl number
p = static pressure
$\boldsymbol{Q}$ = conserved variable vector
$\boldsymbol{q}$ = heat transfer vector
Re = Reynolds-number
S = strain rate
$\boldsymbol{S}$ = area vector
$u^+ = u/u_\tau$ = turbulent dimensionless velocity
$u_\tau = \sqrt{\tau_w/\mu_\ell}$ = friction velocity
V = volume
$\boldsymbol{v} = \{u, v, w\}$ = Cartesian velocity vector
$y^+ = y\rho u_\tau/\mu_\ell$ = turbulent dimensionless distance
α = angle of attack
δ = Kronecker delta
ϵ = dissipation-rate
ϵ^* = homogeneous dissipation-rate
μ = dynamic viscosity coefficient
ρ = density
τ^ℓ = shear-stress tensor
τ^t = Reynolds-stress tensor
ω = turbulent frequency

Subscript

$i = \{x, y, z\}$ = indices used within the Einstein indexing notation
i, j = array indexing
i, m = control volume indices
ℓ = laminar
t = turbulent
w = wall
∞ = freestream

Superscript

$''$ = turbulent fluctuation

I. Introduction

THE present paper reports on recent improvements on a three-dimensional (3-D), unstructured-mesh, finite-volume method for complex aerospace applications developed by the CFD group at Instituto de Aeronáutica e Espaço (IAE). The objective of the CFD group at IAE is to develop the capability of simulating 3-D, viscous turbulent flows over general launch vehicle configurations. Viscous simulations at high Reynolds numbers are typical for aerospace applications, such as the ones of interest to IAE, and turbulence is certainly important for these flow regimes. The correct modeling of turbulence effects in aerospace flows is decisive for consistent computation of complex phenomena such as boundary layers subjected to adverse-pressure gradients, boundary-layer/shock-wave interactions, wing wakes, mixing layers, and others. Such phenomena strongly affect the final aerodynamic result, including even the macro quantities that are usually enough for engineering purposes, such as integrated lift and drag coefficients.

The current code has already been used to simulate turbulent viscous flows over typical aerospace configurations with linear eddy-viscosity turbulence models (EVMs), with acceptable results so far [1]. For such effort, the Spalart–Allmaras (SA) [2] one- and the shear-stress transport (SST) [3] two-equation turbulence models have been chosen. Some less acceptable results, however, have been found

---

Presented as Paper 2826 at the 24th AIAA Applied Aerodynamics Conference, San Francisco, CA, 5–8 June 2006; received 15 December 2006; revision received 24 February 2007; accepted for publication 5 April 2007.

[*] Ph.D. Student, Centro Técnico Aerospacial; enda.bigarella@gmail.com.

[†] Senior Research Engineer, Centro Técnico Aerospacial; currently Director for Space Transportation and Licensing, Brazilian Space Agency, Brasília, Brazil; azevedo@iae.cta.br. Associate Fellow AIAA.

when strong interactions between shock wave and turbulent boundary layer were present in the flow field [4]. Flight conditions with shock waves are certainly of primary concern at IAE, and the results obtained for boundary-layer/shock-wave interactions motivated further effort on this subject.

The scientific community has been directing more attention to the issue of boundary-layer/shock-wave interactions in the last decade. The authors believe that such renewed interest is associated with previous restrictions on computational resources for such complex flow phenomenon simulation, as well as the proper understanding of the turbulence phenomena when interacting with shock waves. Some key work on this subject can be found in [5–12]. Although no definite solution can be found in such work, at least some guidelines for successful simulation of such a flow phenomenon with adequate results for engineering purposes can be collected. One of the outstanding remarks from such work is that, most preferably, researchers focus on advanced turbulence closures, such as Reynolds-stress models (RSMs) or their explicit algebraic (EARSM) derivatives, to tackle the issue of boundary-layer/shock-wave interaction. The main reason for that is the ability of such closures to handle turbulence anisotropy, which seems to be an important feature in shock-wave and boundary-layer interaction, as well as separated flows, flows subjected to adverse-pressure gradients, and other complex phenomena. However successful results can also be obtained with EVM options.

Therefore to enhance the current numerical tool with more advanced turbulence-modeling capabilities, further extension of the code included other turbulence models than the SA and SST models previously available. Other EVM options, such as the realizable k–ϵ [13] and the low-Reynolds-number k–ω [14] models, have been considered. A nonlinear formulation resulting from an EARSM [15,16] is also considered. For completeness of the modeling effort, two RSMs are included. Their formulation naturally offers the potential for more reliable prediction of the turbulence effects because important terms are exactly treated. The high-Reynolds-number Menter StressBSL and the low-Reynolds-number Craft–Launder [8] RSMs are currently considered.

Extensive verification and validation of this code had already been initiated [1,17,18]. In [18], especially, a detailed study of verification and numerical accuracy of the present numerical tool is presented. In the present paper, turbulence model results are validated for a zero-pressure-gradient flat-plate and a parallel-wall channel flow cases. Numerical results are compared with either experimental or direct numerical simulation (DNS) results. Extensive results are, then, presented for transonic flow conditions over a supercritical airfoil. Simulation results are compared with available wind-tunnel experimental data. In general, acceptable numerical results are obtained.

This introduction section describes the motivation for the current effort. In the second section of this paper, the theoretical and numerical formulations embedded in the numerical tool are briefly presented. In the third section, a summary of the currently considered linear eddy-viscosity turbulence models is presented. Similar discussion for the chosen Reynolds-stress models is performed in the fourth section. A careful evaluation of numerical simulation results is presented in the fifth section. A concluding remark section closes the paper with the major conclusions obtained from the current effort.

II. Theoretical and Numerical Formulations

A. Reynolds-Averaged Navier–Stokes Equations

The flows of interest in the present context are modeled by the 3-D compressible Reynolds-averaged Navier–Stokes (RANS) equations, written in dimensionless form and assuming a perfect gas, as

$$\frac{\partial \boldsymbol{Q}}{\partial t} + \nabla \cdot (\boldsymbol{P}_e - \boldsymbol{P}_v) = 0, \qquad \boldsymbol{Q} = \begin{bmatrix} \rho & \rho u & \rho v & \rho w & e \end{bmatrix}^T \tag{1}$$

The inviscid and viscous flux vectors are given as

$$\boldsymbol{P}_e = \begin{Bmatrix} \rho \boldsymbol{v} \\ \rho u \boldsymbol{v} + p\hat{\mathbf{1}}_x \\ \rho v \boldsymbol{v} + p\hat{\mathbf{1}}_y \\ \rho w \boldsymbol{v} + p\hat{\mathbf{1}}_z \\ (e+p)\boldsymbol{v} \end{Bmatrix}, \qquad \boldsymbol{P}_v = \frac{1}{Re} \begin{Bmatrix} 0 \\ \left(\tau^{\ell}_{xi} + \tau^{t}_{xi}\right)\hat{\mathbf{1}}_i \\ \left(\tau^{\ell}_{yi} + \tau^{t}_{yi}\right)\hat{\mathbf{1}}_i \\ \left(\tau^{\ell}_{zi} + \tau^{t}_{zi}\right)\hat{\mathbf{1}}_i \\ \beta_i \hat{\mathbf{1}}_i \end{Bmatrix} \tag{2}$$

The shear-stress tensor is defined by

$$\tau^{\ell}_{ij} = \mu_{\ell}\left[\left(\frac{\partial u_i}{\partial x_j} + \frac{\partial u_j}{\partial x_i}\right) - \frac{2}{3}\frac{\partial u_m}{\partial x_m}\delta_{ij}\right] \tag{3}$$

where u_i is the Cartesian velocity component and x_i is the Cartesian coordinate. The viscous force work and heat transfer term β_i is defined as $\beta_i = \tau_{ij}u_j - q_i$, where the heat transfer component is defined as

$$q_j = -\gamma\left(\frac{\mu_{\ell}}{Pr} + \frac{\mu_t}{Pr_t}\right)\frac{\partial(e_i)}{\partial x_j} \tag{4}$$

It is important to remark here that for the flow conditions of interest here, the Reynolds analogy for the turbulent heat transfer, as considered in Eq. (4), is adequate and numerically robust. The molecular dynamic viscosity coefficient μ_{ℓ} is computed by the Sutherland law [19]. The dimensionless pressure can be calculated from the perfect gas equation of state.

This set of equations is solved according to a finite-volume formulation. For convective-flux calculations on the volume faces, a Roe flux-difference splitting scheme [20] is currently used. To achieve a second order of accuracy in space, properties are linearly reconstructed in the faces based on the MUSCL [21] algorithm. The implementation follows a modified and generalized Barth and Jespersen [22] multidimensional limiter formulation [18]. The van Albada [18] limiter is used to avoid oscillations near discontinuities. Diffusive-flux terms are discretized based on a usual centered scheme, with properties in the faces obtained as an arithmetical average of the properties in the neighboring cells. Flow equations are integrated in time by a fully explicit, second-order accurate, five-stage, Runge–Kutta time stepping scheme. An agglomeration full-multigrid scheme is included to achieve better convergence rates for the simulations. More details on the theoretical and numerical formulations can be found in [1,18].

B. Turbulence Modeling

The turbulence effects are included into the RANS equations by the Reynolds-stress tensor, defined by

$$\tau^{t}_{ij} = -Re\overline{\rho u''_i u''_j} \tag{5}$$

Various turbulence models are available in the current code, ranging from linear and nonlinear eddy-viscosity models, to Reynolds-stress models. The model transport equations are also solved according to the finite-volume approach. The time march is performed using an implicit Euler scheme [17].

For the discretization of the advection term it is normally recommended to use dissipative upwind discretization schemes to avoid oscillations near discontinuities. A first-order upwind scheme is currently chosen

$$\int_V \nabla \cdot (\rho q \boldsymbol{v})\, \mathrm{d}V \approx \frac{1}{V_i}\sum_{k=1}^{nf}\left[v^{+}_{n_k}(\rho q)_i + v^{-}_{n_k}(\rho q)_m\right]|\boldsymbol{S}_k| \tag{6}$$

where the kth face is shared by the ith and mth cells, nf is the total number of faces for the ith cell, $\boldsymbol{S}_k$ is the area vector for the kth face, and q is a generic transported property, here taken to represent a generic turbulent quantity. The velocity components are defined as

$$v^{+}_{n_k} = (v_{n_i} + |v_{n_i}|)/2, \qquad v^{-}_{n_k} = (v_{n_m} - |v_{n_m}|)/2 \\ v_n = \boldsymbol{v} \cdot \boldsymbol{S}_k / |\boldsymbol{S}_k| \tag{7}$$

For the discretization of the diffusion term an usual centered-scheme approach showed to be extremely unstable, allowing for large oscillations to build up. An alternative method to compute nonoscillatory derivatives in the face is currently proposed as an approximate finite difference scheme. This approximation uses the adjacent cell centroid property and relative distance to build the derivative in the face as

$$\nabla q_k = \frac{q_m - q_i}{|\boldsymbol{d}_k|} \frac{\boldsymbol{d}_k}{|\boldsymbol{d}_k|}, \qquad \boldsymbol{d}_k = \boldsymbol{r}_m - \boldsymbol{r}_i \tag{8}$$

where $\boldsymbol{d}_k$ is the distance vector between the centroids of the cells that share the kth face.

III. Eddy-Viscosity Turbulence Models

Eddy-viscosity models compute the Reynolds stresses [Eq. (5)] through the Boussinesq hypothesis, which states that the turbulence stresses are a linear function of the mean flow straining rate times a modifying constant such as

$$\tau_{ij}^t = 2\mu_t S_{ij} - \frac{2}{3}\rho k \delta_{ij} \tag{9}$$

$$S_{ij} = \frac{1}{2}\left(\frac{\partial u_i}{\partial x_j} + \frac{\partial u_j}{\partial x_i}\right) - \frac{1}{3}\frac{\partial u_m}{\partial x_m}\delta_{ij} \tag{10}$$

where μ_t is the eddy-viscosity coefficient computed by the chosen turbulence model.

A. Spalart–Allmaras Model

The Spalart–Allmaras single equation model [2] solves a transport equation for a modified eddy-viscosity coefficient. Its transport equation can be integrated to the wall without any numerical difficulty provided that $y^+ \approx 1$ near the wall. The model is derived along intuitive, empirical lines, heavily relying on calibration by reference to a wide range of experimental data and on the knowledge of the distance to the wall. The model has been applied without any further modification by the CFD community for 3-D compressible flows with good results so far [11,23] in shock-induced separations and adverse-pressure gradient boundary layers. Because this model does not make use of the turbulent kinetic energy k, the last term in Eq. (9) is assumed zero.

B. Shear-Stress Transport Model

Further improvement on the high-Reynolds-number Wilcox k–ω model can be obtained with the Menter SST model [3,24]. The SST model is derived from a blend of the original k–ω [25] and the standard k–ϵ [26] models. It solves reported problems of the k–ω closure regarding freestream value dependency [24] while keeping the better numerical behavior of this model close to the wall. Model constants are generally calculated as $\phi = F_1\phi_1 + (1 - F_1)\phi_2$, where ϕ_1 represents the set of constants for the k–ω model and ϕ_2, the set for the standard k–ϵ model, as in [24]. The F_1 variable is a blending function that turns on the k–ω closure near solid walls and the standard k–ϵ model outside boundary layers, and it is dependent on the distance to the wall.

It is known in the CFD community that standard two-equation models are not capable of accurately computing adverse-pressure gradients or separated flows [3]. These models require a stronger pressure gradient or a longer running length to separate than is indicated by experiments. It is demonstrated that this is a result of the missing effect of turbulent shear-stress transport in this type of flow [27]. To take the shear stress into account, at least in an ad hoc fashion, the eddy-viscosity coefficient for the SST model is bounded by a measure of the flow strain rate [24]. Another blending function is used to turn on this criterion only inside boundary layers. A careful discussion on the motivations for this procedure can be found in [3].

A simpler version of the SST model, denoted as the BSL model [3], exactly follows the above formulation, however, without the last criterion for the eddy-viscosity coefficient [3]. Both BSL and SST models can be integrated to the wall when $y^+ \approx 1$ near the wall.

C. Low-Reynolds-Number Wilcox k–ω Model

The k–ω (WKOM) model is an empirical closure based on transport equations for k and ω [25]. This model has been developing over the years including corrections and improvements to a wide range of different flow cases. Its low-Reynolds-number version, also modified for improved accuracy in free-shear flows, as in [14], is used in the present work. The model is closed with constants [14] obtained from calibration against key test cases for turbulent flows [25]. Its transport equation can also be integrated to the wall if the condition of $y^+ \approx 1$ near the wall is satisfied.

D. Realizable k–ϵ Model

The realizable k–ϵ (RKE) model [13] solves transport equations for k and ϵ. A realizable estimate of the turbulent time scale based on the local turbulent Reynolds number, removes the stiffness of the original k–ϵ model [26] near solid walls. An additional term in the dissipation-rate equation is considered to improve the model response to adverse-pressure gradient regions. The eddy-viscosity coefficient is bounded following a Schwarz inequality realizability criterion [13]. In that definition, a low-Reynolds-number damping function, designed to account for the damping of turbulent fluctuations near solid walls, is also available. These features compose a model that does not require the distance to the wall and that can be integrated through the whole boundary layer provided that $y^+ \approx 1$ near the wall.

IV. Reynolds-Stress Turbulence Models

A. General Considerations

Reynolds-stress models use the exact equations for the transport of Reynolds stresses obtained by taking velocity-weighted moments of the Navier–Stokes equations and neglecting density fluctuations. The general form of a RSM is given by

$$\frac{D\rho\overline{u_i''u_j''}}{Dt} = P_{ij} + D_{ij}^v + D_{ij}^t + D_{ij}^p + \Phi_{ij}^* - \epsilon_{ij} \tag{11}$$

with the individual terms representing specific turbulence mechanisms, where P_{ij} is the turbulent production; D_{ij}^v is the molecular diffusion; D_{ij}^t is the turbulent diffusion; D_{ij}^p is the pressure diffusion; Φ_{ij}^* is the pressure–strain correlation; and ϵ_{ij} is the turbulent dissipation. The turbulent production and the molecular diffusion terms do not require modeling. The representation of the remaining terms is model dependent and they are briefly discussed separately in the respective following subsections.

RSMs also require the solution of another transport equation for a measure of the turbulent length scale, usually represented by a turbulent kinetic energy dissipation quantity. Examples of such quantities are the dissipation ω or the scalar dissipation rate, ϵ, of k. The estimation of those quantities is perhaps the weakest point in Reynolds-stress modeling.

B. Modified Craft–Launder RSM

The modified Craft–Launder RSM (CLMRSM) closure is a variation of the nonlinear RSM in [28], which does not require wall-topology parameters such as normal-to-wall vectors and distance from the wall. Modifications of some wall-proximity corrections have been applied to correct the latter model incorrect response to shock waves, which were falsely interpreted as regions of strong inhomogeneity [8].

The pressure–strain correlation is considered a critical element for RSMs because it can be of the order of the production and dissipation terms, hence playing a crucial role in most flow cases. Instead of a wall-normal vector, which can cause problems for complex geometry applications, two turbulence inhomogeneity indicators based on gradients of the turbulent length scale and Lumley's flatness parameter [29] are used. A cubic pressure–strain model is here used in conjunction with additional coefficients and those inhomogeneity corrections. This option allows for integration through the viscous sublayer and acts consistently through shock waves, which is an important feature for the flows of interest to IAE.

The generalized gradient diffusion hypothesis (GGDH) in [30] is used for the modeling of the turbulent diffusion. A thin-layer approximation of that term, as in [8], is used here to avoid numerical instabilities in distorted cells. The pressure diffusion is also considered. It is modeled based on inhomogeneity-indicator vectors and Lumley's stress-flatness parameter.

The dissipation tensor blends isotropic and wall-limiting terms, with an additional term to account for the dip in the shear-stress dissipation rate in the buffer layer. An equation for the homogeneous dissipation rate ϵ^* is used to determine ϵ. This equation incorporates a few modifications to better match low-Reynolds-number effects near solid walls [8].

C. StressBSL RSM

This option uses a linear pressure-correlation model considering the contributions from [31,32]. Because viscous dissipation occurs at the smallest scales, most high-Reynolds-number models, as the current one, employ the local isotropy hypothesis of Kolmogorov [26]. The pressure diffusion is here neglected, as usual in RSMs. The turbulence-length-scale determining equation is based on the Menter BSL ω equation [3]. This set of equations composes a high-Reynolds-number turbulence closure.

D. Wallin–Johansson EARSM (NLBSL)

The main motivation in the development of EARSMs is the general need for improvements in the prediction of complicated turbulent flow phenomena using the platform of existing CFD codes based on two-equation eddy-viscosity turbulence-modeling capability. This is an interesting way of cheaply incorporating advanced turbulence effects, such as streamline curvature and normal stress separation, into an already existing two-equation turbulence model framework, avoiding thus the large amount of computational resources required by the solution of RSMs.

The classical algebraic RSM (ARSM) starts by assuming equilibrium turbulence, which is equivalent to neglecting advection and diffusion for the transport equations of the Reynolds-stress anisotropy tensor. In the formulation in [15], an isotropic assumption for the dissipation tensor along with a linear pressure–strain correlation are chosen. Substituting those terms into the ARSM, one gets an implicit algebraic equation for the Reynolds-stress anisotropy tensor. The solution of this implicit equation is numerically cumbersome and, thus, a general form for the anisotropy tensor in terms of strain and rotation tensors is proposed [15]. This general form for the anisotropy tensor implies the use of initially unknown coefficients.

The explicit solution for the anisotropy tensor now relies on the determination of these coefficients. Some researches adopt the approach of calibrating those terms to a set of representative turbulence problems [33]. This approach, however, may decrease the generality of the additional nonlinear Reynolds-stress tensor components. The approach in [15] substitutes the anisotropy tensor expansion in the implicit ARSM equation. A solution to the unknown expansion coefficients can, thus, be found as detailed in that work. The compressible formulation along with an ad hoc modification to recast, at least qualitatively, the initially neglected diffusion, as available in [15], is chosen in the present work.

The EARSM is implemented as a plug-in for the BSL background model. The nonlinear Reynolds stresses are provided by the proposed tensor expansion such as

$$-\rho\overline{u_i'' u_j''} \approx 2C_\mu^{\mathrm{eff}}\frac{\rho k^2}{\epsilon}S_{ij} - \frac{2}{3}\rho k\delta_{ij} - \rho k a_{ij}^{nl} \tag{12}$$

The first two terms in the RHS of the previous equation are similar to those used for linear models, derived from the Boussinesq hypothesis. An effective eddy-viscosity coefficient C_μ^{eff}, however, is adopted. This coefficient is one of the major contributions of EARSMs because it adapts to the local strain and vorticity fields, which, for instance, removes the need for the strain-rate-based bound in the eddy-viscosity definition of the SST model. The remaining *anisotropic* contribution is wrapped in the a_{ij}^{nl} tensor [15].

The BSL equation is designed in conjunction with the linear constitutive Boussinesq hypothesis. This fact can compromise the performance of the model if rather combined with a nonlinear closure. To circumvent these limitations, the recommended approach is a complete recalibration of the BSL model along with the added EARSM nonlinear terms [16,34]. In the referenced work, a variable C_μ coefficient, rather than the constant one of the original BSL model, is considered in the recalibration process. This option guarantees a more consistent representation of turbulence fields under the EARSM nonlinear formulation [16].

V. Results and Discussion

A. Initial Discussion

Linear turbulence models are developed considering effects that are essentially linked to the shear stress in the local streamwise direction. Such effects are, for instance, the skin friction or the effect of the boundary-layer displacement into the outer irrotational flow. Isotropy of normal stresses is assumed along a streamline because, in a simple shear flow, which usually serves as a calibration milestone for linear EVMs, the normal stresses are dynamically inactive, not contributing to the momentum balance.

The response of the boundary layer to adverse-pressure gradient or streamline curvature is, however, dictated by the shear stress as well as the normal stresses. In that case, normal stresses are dynamically active, and they also work toward sensitizing the shear stress to the normal straining (as through a shock wave) and curvature. More than that, yet, the shear stress is generated by an interaction between the crossflow normal stress and the local flow straining. Near the wall, strong anisotropy is found, where the streamwise normal stress is generated by local flow shear straining, and other normal stresses are fed by the redistributive pressure–strain correlation, which tends to steer turbulence toward isotropy. Those aspects emphasize the need for all turbulence models to return realistic levels of anisotropy.

From a detailed analysis of the production definition for linear EVMs [24], it is possible to observe that the flow straining appears squared. The resulting net effect is that flow straining always works to elevate the normal stresses, irrespective of the sign of the strain. This lends to largely overpredicted turbulence production for highly strained flows. This approximation is not capable of transmitting the negative crossflow normal stress production in the case of a boundary layer in a convex wall, with accentuated streamline curvature, for example.

These effects are addressed in the test cases to come. Typical turbulent aerodynamic flows are considered to evaluate the currently chosen turbulence model capabilities with focus on the previous discussions. Turbulence modeling is verified with a 2-D flat plate and a plane-symmetric channel flow experiments. Transonic flows about a supercritical airfoil, with strong interaction between shock wave and boundary layers, are also presented. The effect of anisotropy resolution in the mean flow results is carefully assessed.

B. Zero-Pressure-Gradient Flat Plate

1. *Initial Remarks*

The turbulent incompressible flow over a zero-pressure-gradient flat-plate configuration is addressed. This is an interesting test case because an analytical solution for the averaged turbulent boundary layer [35] is available. This solution is known in the literature as the log–law profile. Experimental data are also available for this test case [36,37]. Numerical simulation results are compared with both log–law and experimental data.

Most of turbulence models are calibrated against this classical shear flow case, among other flows, as well. This is also the case for the closures chosen for the present work. Therefore these turbulence models are expected to approximate the numerical solution of the turbulent flat-plate flow to the log–law profile. The reader should keep in mind that this analysis, however, is not enough to extend the turbulence model performance for more complicated flows, with turbulence and mean flow structures other than shear-stress effects as in this validation case. For other complex flows, it is necessary to compare numerical solutions to available experimental data to coherently evaluate the applicability of the model. Such studies are performed in the sections to come.

In the flat-plate case, the freestream Mach number is set to $M_\infty = 0.20$ to approximate the numerical solution to an incompressible flow situation. Because the present code has only a compressible formulation, it is not advisable to lower the freestream Mach number below that value on behalf of still acceptable convergence levels [38]. The Reynolds number per unit plate length is set to 10.3×10^6.

Two computational meshes are considered, with a different number of cells along the boundary-layer height, namely 60 and 100 cells. Both meshes are built with 20 cells outside the boundary-layer height, and with 68 cells along the flat-plate length, with the mesh starting along with the flat-plate leading edge. The normal direction from the wall is stretched with an exponential growth of 10% in the laminar sublayer, and the meshes are also clustered near the stagnation region to guarantee accuracy for the high gradients expected there. This grid configuration yields a suitable computational mesh for turbulent flow simulations over the flat plate in the sense of the turbulence-modeling validation work presented in [39]. In other words, the computational meshes guarantee $y^+ \approx 1$ for the first mesh point away from the wall, as is verified in the forthcoming analyses. At least 60 grid points inside the fully developed turbulent boundary layers, as well as about 10 grid points inside the viscous and buffer sublayers, are also observed.

Simulations are carried out with a multigrid configuration using "V" cycles, with one smoothing iteration at each grid level, and $CFL = 1.5$. SA, SST, RKE, WKOM, NLBSL, CLMRSM, and StressBSL turbulence models are considered in the simulations. Mesh dependency is analyzed for the SST model with the two prescribed meshes. The resulting grid to which mesh-independent solutions are found is chosen for the other turbulence models. All simulations are stopped to either a maximum x-momentum residue drop of 7 orders of magnitude, or to convergence of the integrated skin friction coefficient.

2. *Boundary-Layer Analyses*

In Fig. 1, numerical boundary layers obtained with the indicated turbulence model are compared with the theoretical log law and the experimental data of [37], for a given section along the flat-plate longitudinal direction with local Reynolds number $Re_x = 7.62 \times 10^6$. This comparison is made in terms of $u+$, where u_τ is taken from the experiment, and y^+. Detailed definitions for $u+$ and y^+ can be found in [35]. All simulations are carried out on the mesh with 60 points inside the boundary layer, which showed to provide adequately mesh-independent solutions in general.

One can observe in the results in Fig. 1 a good agreement of the numerical results with the theoretical and experimental data. The results slightly differ in the inertial layer, but the laminar sublayer and the boundary-layer thickness are well predicted by all models, except for WKOM. It is natural that models differ in the inertial layer because this region is intrinsically related to the von Karman constant κ value used in the model calibration [35]. This constant is directly obtained from experiments, and a range of value is usually found [35]. The model developer picks the value he or she finds most suitable, and hence the numerical boundary layer results may naturally differ.

Further comparisons are also made with the experimental results of [36]. Differently than the data in [37], the results in [36] are provided in terms of absolute quantities and not in terms of u^+ and y^+ variables. This option avoids the experimental uncertainties related to the determination of u_τ. In Fig. 2, numerical boundary layers are compared with the experimental data of [36], for a given section along the flat-plate longitudinal direction with local Reynolds number $Re_x = 4.2 \times 10^6$. Boundary layers are plotted with the dimensionless velocity u/U_e, where U_e is the freestream velocity, against the distance from the wall in terms of the experimental reference length. It is interesting to observe that all models accurately predict boundary-layer profiles and thickness, except for WKOM, which overpredicts the boundary-layer thickness.

3. *Shear Reynolds-Stress Analyses*

Another interesting result that is helpful in the assessment of the turbulence models is the Reynolds-stress shear component $\overline{u''v''}$. Experimental results for this quantity are also available in [36]. In Fig. 3, shear-stress profiles are presented for the turbulence models considered in the present effort, and compared with the experimental results. In these results, greater differences in the model behavior can be observed. SST, NLBSL, and StressBSL models slightly underpredict the shear stress levels, whereas WKOM underpredicts its peak and overpredicts the turbulence intensities outside the boundary layer. RKE slightly overpredicts the shear stresses. Finally SA and CLMRSM models strikingly match the experimental data. The small differences between numerical and experimental data for SST, NLBSL, StressBSL and RKE models do not seem to be decisive in these cases, because very acceptable boundary-layer results are observed in Figs. 1 and 2.

It is interesting to remark here that further analyses, not shown here to avoid overloading this section, indicate larger dependency of CLMRSM with near-wall grid refinement and topology, especially in terms of y^+. For this model, the shear-stress result is mesh independent for a grid with $y^+ \approx 0.5$ and 90 cells within the boundary layer. The CLMRSM results in Fig. 3 are presented for that grid configuration. However the good boundary-layer results in Figs. 1 and 2 are obtained with the same grid configuration as for the other models in that case. The more refined grid for CLMRSM also presents better results in terms of friction drag, as analyzed in the section to come.

4. *Friction Drag Analyses*

The shearing of the flow over the flat plate creates the friction drag component. This is a local quantity, in the sense that each longitudinal station along the flat plate has a local friction drag component. In Fig. 4, the numerical c_f distributions for each turbulence model already described are compared with the experimental results from [37]. It can be observed that all models predict friction coefficient distributions within reasonable bounds around the experimental data. The ω-based SST, NLBSL, and StressBSL models strikingly match the experimental distribution. Other models slightly overpredict the friction coefficient distributions.

It is also interesting to observe in Fig. 4 that all two-equation EVMs and RSMs predict a small transition length near the flat-plate leading edge, which is represented by the region upstream the peak in c_f downstream the plate leading edge. Although the prediction of a transitional region is a native property of such advanced models, this region, however, should not be regarded as a correct transitional length because these closures are not actually calibrated for this matter. Hence, the resulting numerical transition length is nonphysically dependent on the far-field turbulence boundary conditions.

5. *Computational Resource Usage*

Another important aspect regarding turbulence modeling that should certainly be emphasized here is the increase in the computational resources necessary to solve the new equations added to the formulation. The SA costs per iteration are about 1.5 times larger than those for a laminar simulation of the present flat-plate case. Two-equation model figures, including NLBSL, are slightly higher, amounting to about 5% over the SA simulation. One should observe that the NLBSL approximation costs about the same as the SST model although providing higher physical consistency, as discussed in the sections to come. This advantage is exactly the motivation for the development of the EARSM class of turbulence

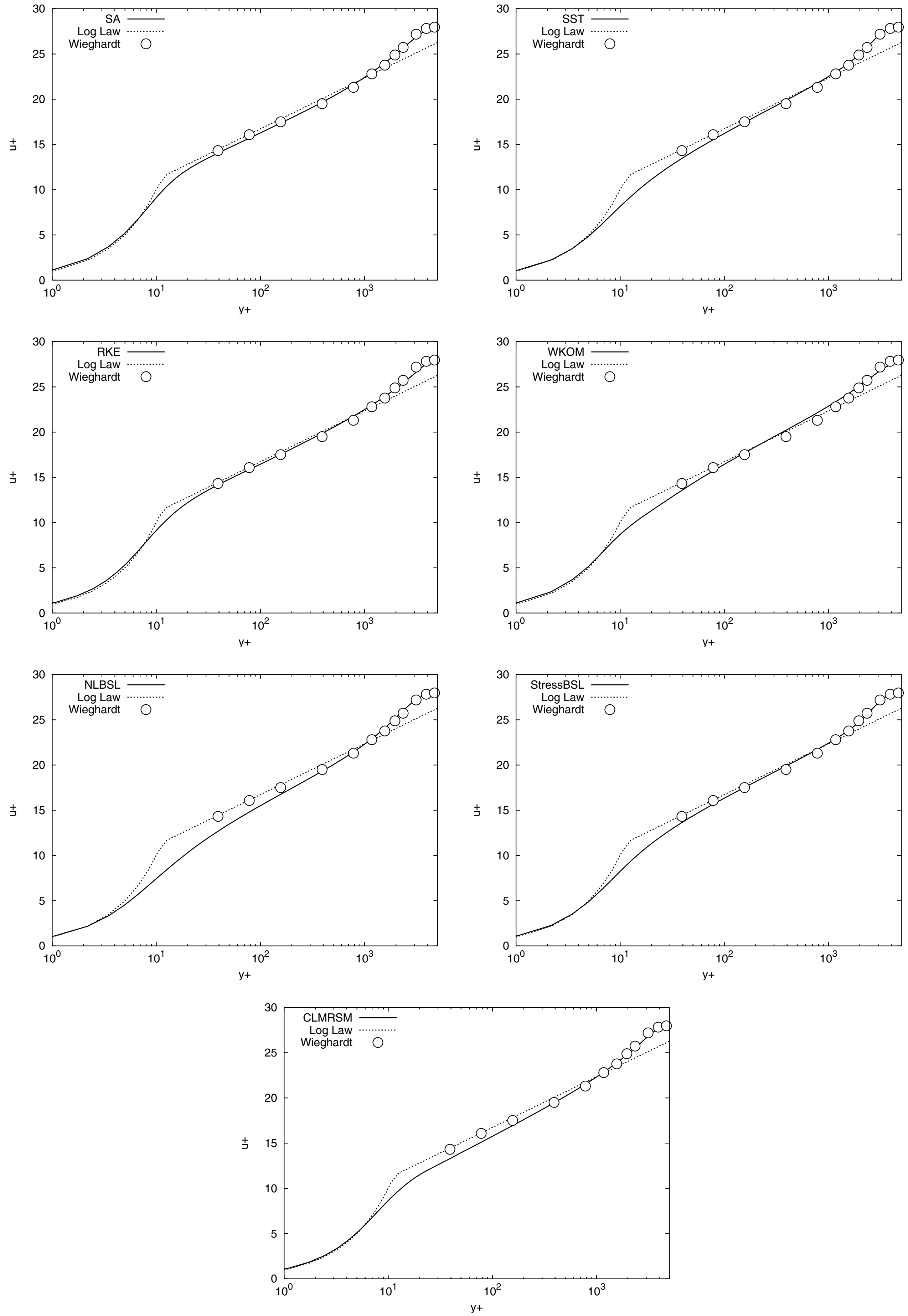

Fig. 1 Numerical, theoretical, and experimental [37] turbulent boundary layers for a zero-pressure-gradient flat-plate flow ($Re = 7.62 \times 10^6$).

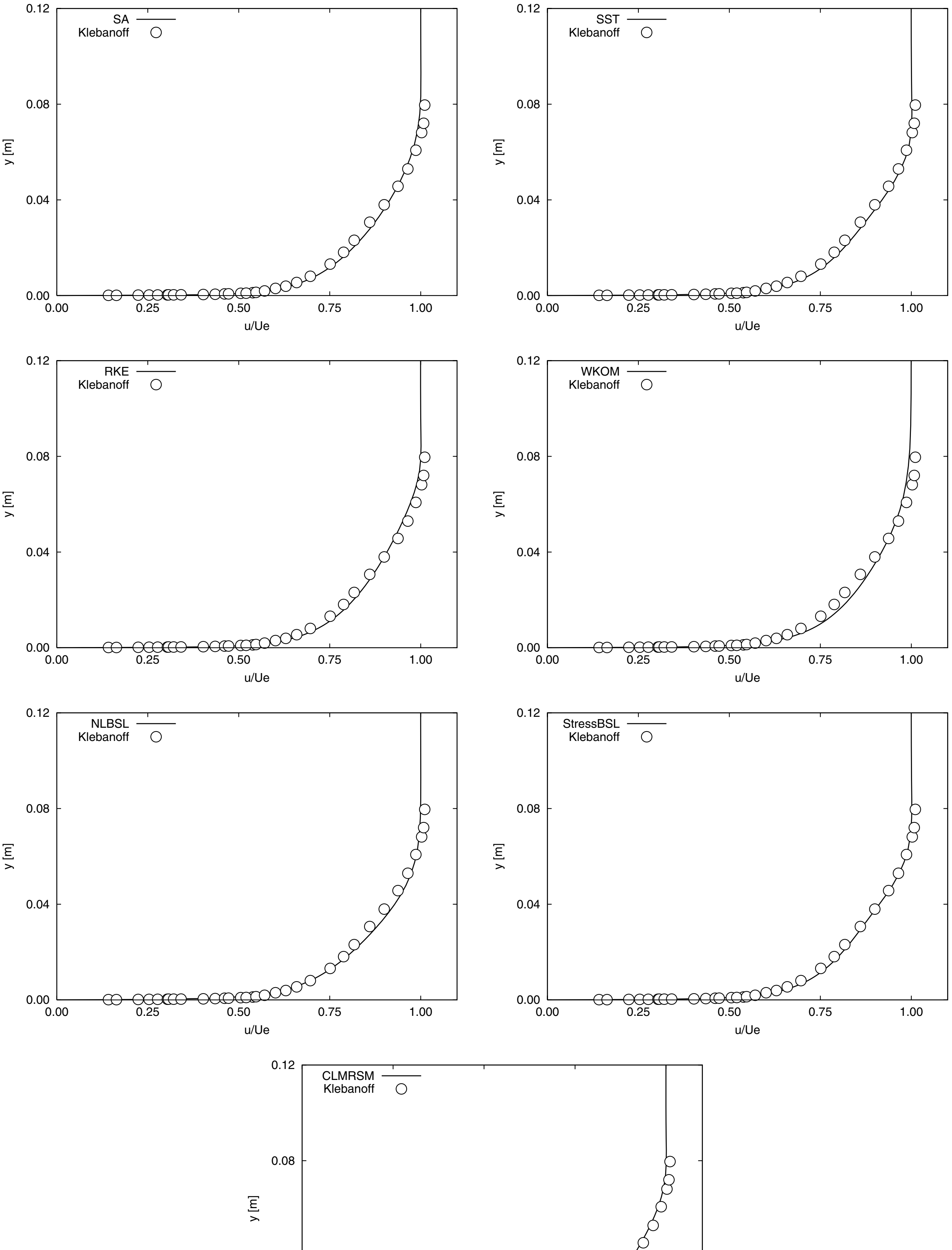

Fig. 2 Numerical and experimental [36] turbulent boundary layers for a zero-pressure-gradient flat-plate flow ($Re = 4.2 \times 10^6$).

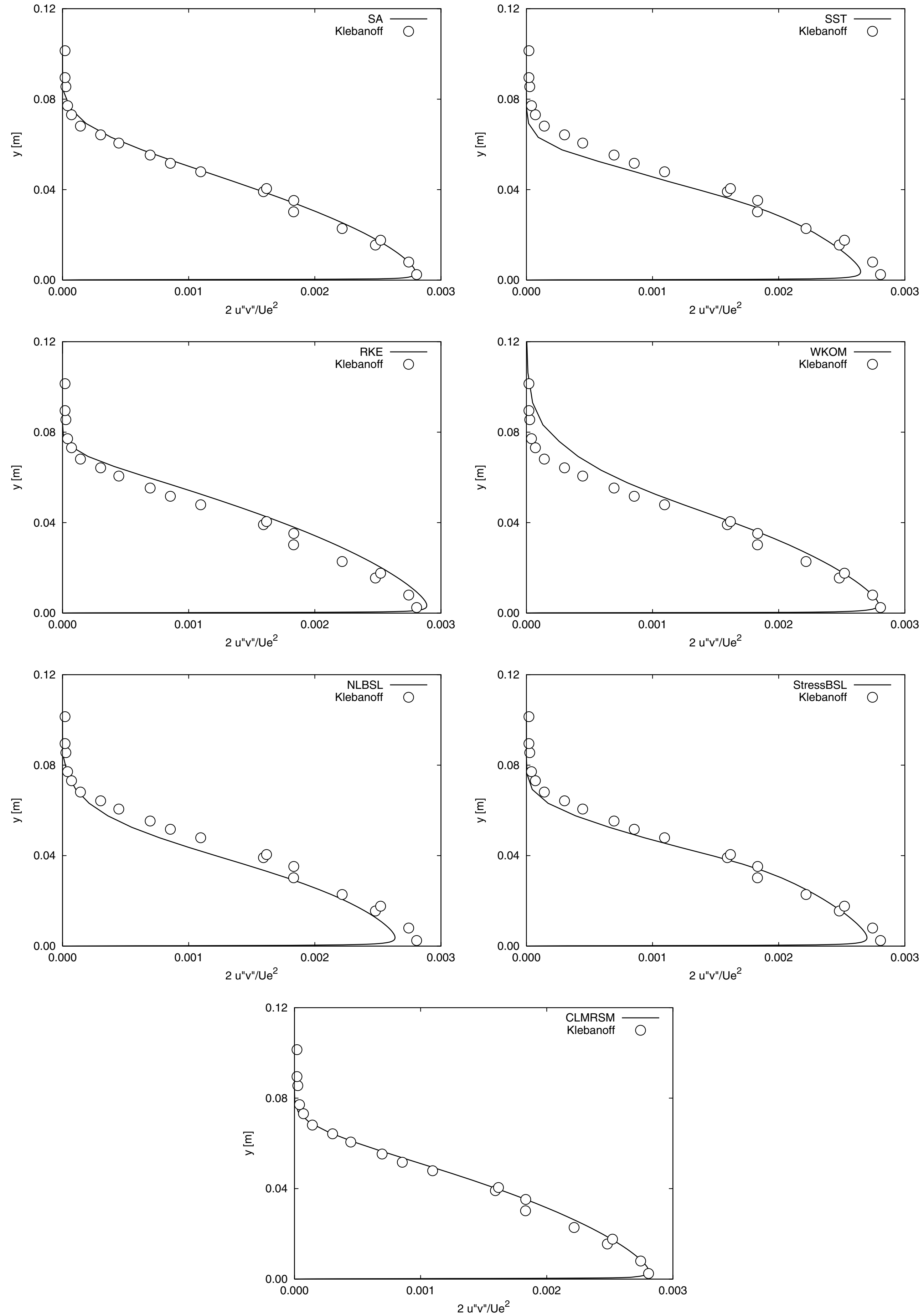

Fig. 3 Numerical and experimental [36] Reynolds-stress shear component for a zero-pressure-gradient flat-plate flow ($Re = 4.2 \times 10^6$).

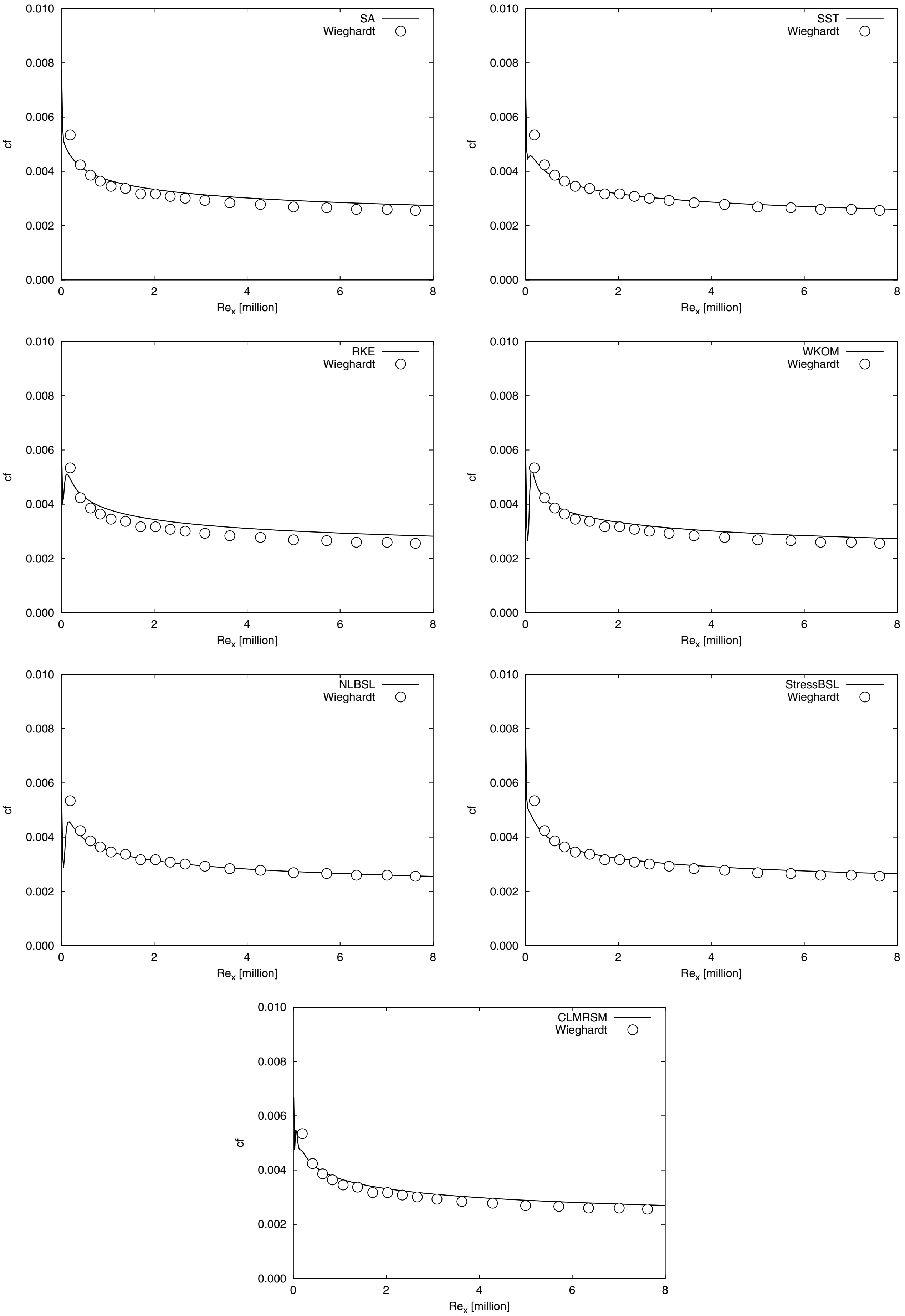

Fig. 4 Numerical and experimental [37] local friction drag coefficient distributions for a zero-pressure-gradient flat-plate flow.

models, as already pointed out in the current work. Reynolds-stress models, on the contrary, solve seven additional turbulence transport equations for a 3-D case, resulting in larger resource overheads. StressBSL costs rise up to 25%, and CLMRSM reaches almost 130% times the resources for a SA model simulation. It is expected larger physical advantages for this class of model to compensate the much higher computational resource usage.

C. Fully Developed Channel Flow

1. Initial Remarks

Although the mean boundary layer of a fully developed parallel-wall channel flow case also respects the log–law solution as for the flat-plate case, this still is an interesting test case because DNS results [40] are available for further evaluations. From the DNS results, it is possible to easily and confidently extract important turbulence information such as shear and normal Reynolds stresses. These terms are decisive for successful simulations of complex flow turbulence phenomena, as further discussed. Current numerical results are compared with the DNS data from [40] at friction Reynolds number $Re_\tau = 180$ based on the channel half-height.

2. Mesh Dependency Study

Initially a mesh refinement and topology dependency study is performed for this test case. Six grid configurations are considered, resulting in the following set:

1) 30 cells in the normal direction, with $y^+ = 1.0$;
2) 60 cells in the normal direction, with $y^+ = 0.5$, 1.0 and 2.0;
3) 90 cells in the normal direction, with $y^+ = 1.0$ and 2.0.

Boundary layers obtained with the available turbulence models for this set of grids are presented in Fig. 5. First it can be observed that the boundary layers shown here are insensitive to grid refinement and y^+ settings, including the nonrecommended $y^+ \approx 2$ grids. Second the present results are, in general, in good agreement with DNS data, showing the level of accuracy that can be obtained with the current turbulence models, even for such a low-Reynolds-number case.

The WKOM model presents an unexpectedly lower consistency for the current channel flow conditions. The authors attribute this behavior to a poorer calibration of this model to a lower *net* Reynolds number. By net low Reynolds number, here, the reader should understand the Reynolds number computed by the fixed macro flow quantities, and not the locally varying internal turbulent Reynolds number. The latter is actually the one that differentiates the classes of low- and high-Reynolds-number turbulence models. The former is the one that, for instance, defines the flight Reynolds number of an aircraft.

A similar limitation is also found for the NLBSL closure. In this case, however, the author in [16] clearly states that the recalibration effort is intended for high-Reynolds-number flows. Similar poorer resolution of lower Reynolds-number flows are also found in [16]. This limitation, nevertheless, is absolutely not prohibitive here (and also in the applications in [16]) because very high-Reynolds-number flows are of interest in the current work. The previously shown flat-plate results for this model corroborate the assertion that this model performs well at higher local Reynolds number.

Similar mesh-dependency evaluation is performed for the shear Reynolds stress tensor component, $\overline{u''v''}$. Results for the previous set of grids are presented in Fig. 6. Contrary to the boundary-layer results in Fig. 5, the shear stress presents larger dependency with the grid. The negative impact of $y^+ > 1$ for the turbulence models becomes clear in the results from Fig. 6 . An unphysical peak in turbulence is found under such circumstances. For grids with $y^+ \leq 1$ and at least 60 points within the boundary layer, numerical results can be said to be grid independent for all considered turbulence models. The lower number of points inside the boundary layer, 30 in the present case, also result in poorer Reynolds-stress prediction.

An important conclusion from these results is that all currently considered models are equivalent in terms of mesh requirements. In other words, the same mesh built for a given case can be used along with all turbulence models. This indication represents large time-resource savings in practical applications of the current code because it would not be necessary to build one different mesh for each turbulence model simulation, for a given flow case.

3. Normal and Shear Reynolds Stress Analyses

The channel flow experiment is a very interesting case to address turbulence model Reynolds-stress results because the streamlines are coherently aligned with the Cartesian coordinate system. Present computation and DNS Reynolds stresses are plotted in Fig. 7. A grid configuration that supports mesh-independent results, with 90 points along the wall-normal direction and the wall-nearest node located at $y^+ \approx 1$, is used.

It is interesting to observe in Fig. 7 the already commented fact that the linear EVMs, namely the SA, SST, RKE, and WKOM models, predict isotropic normal stress components, that is $\overline{u''u''} = \overline{v''v''} = \overline{w''w''}$. In the SA case, the normal stresses are actually zero. The nonlinear augmentation of the NLBSL formulation allows for separation of the normal stresses. Because NLBSL is a high-Reynolds-number closure, the normal stresses close to the wall do not match the actual stress distribution. The same behavior is found for the StressBSL RSM. Both closures are high-Reynolds-number models and they predict similar Reynolds stresses. The more advanced low-Reynolds-number CLMRSM model presents much stronger anisotropy and a very good match with DNS data. Although the streamwise normal stress $\overline{u''u''}$ is underpredicted by this model, this is of no impact in this particular flow because the shear stress is only sensitive to the crossflow normal stress $\overline{v''v''}$.

D. OAT15A Supercritical Airfoil

1. Initial Remarks

The interaction between shock waves and boundary layers is of considerable practical importance in transonic and supersonic aerospace vehicle design. For thinner boundary layers, a mild shock wave may have just minimal impact on it, causing a moderate thickening of this boundary layer, and subsequently only small modification of the outer inviscid flow. Stronger shock waves, on the other hand, may cause massive flow separation leading to early wing stall or other adverse effects. The mechanics of such interactions are complex and poorly understood. However it is well known that the interaction is highly sensitive to the boundary-layer turbulence state, and its response to the deceleration caused by the shock wave. The turbulence field is highly anisotropic in that region and it responds differently under shear, normal, or curvature straining. Therefore there lies the importance of consistently modeling the turbulence anisotropy and its sensitivity to those types of straining, as earlier discussed.

To demonstrate the importance of the remarks in the previous discussion, transonic flows over the OAT15A supercritical airfoil [41] are addressed. This configuration is here chosen due to the abundant but also carefully obtained wind-tunnel results. The OAT15A airfoil is a 12.3%-thick supercritical aerofoil for transport aircraft. It is studied within the framework of an ONERA/Aeropastiale joint program devoted to the study of such aeronautical designs. The design point of the airfoil is $M_\infty = 0.73$ and $C_l = 0.65$, and the main feature of the flow is an interaction of boundary layer and shock wave. The wind-tunnel tests were performed in the ONERA/CERT T2 wind tunnel [42] for evaluation of Reynolds-number effects on the airfoil performance. The range of $3–20 \times 10^6$ was addressed using the cryogenic capability of the tunnel. The adaptive top and bottom tunnel walls provided the experiments with quasi-free-air conditions. Sidewall effects were, however, present but taken into account in the correction procedure. T2 tests were also compared with similar experiments performed in S3MA wind tunnel [43] for the same geometry and flight conditions to show the quality of the T2 data.

The T2 experiments mainly concern pressure distributions for a fixed Mach number, namely $M_\infty = 0.724$, various angles of attack and Reynolds numbers, with fixed transition at 7% of the aerofoil chord. Lift forces are measured by a balance, and drag forces are obtained by wake survey at half a chord downstream the profile.

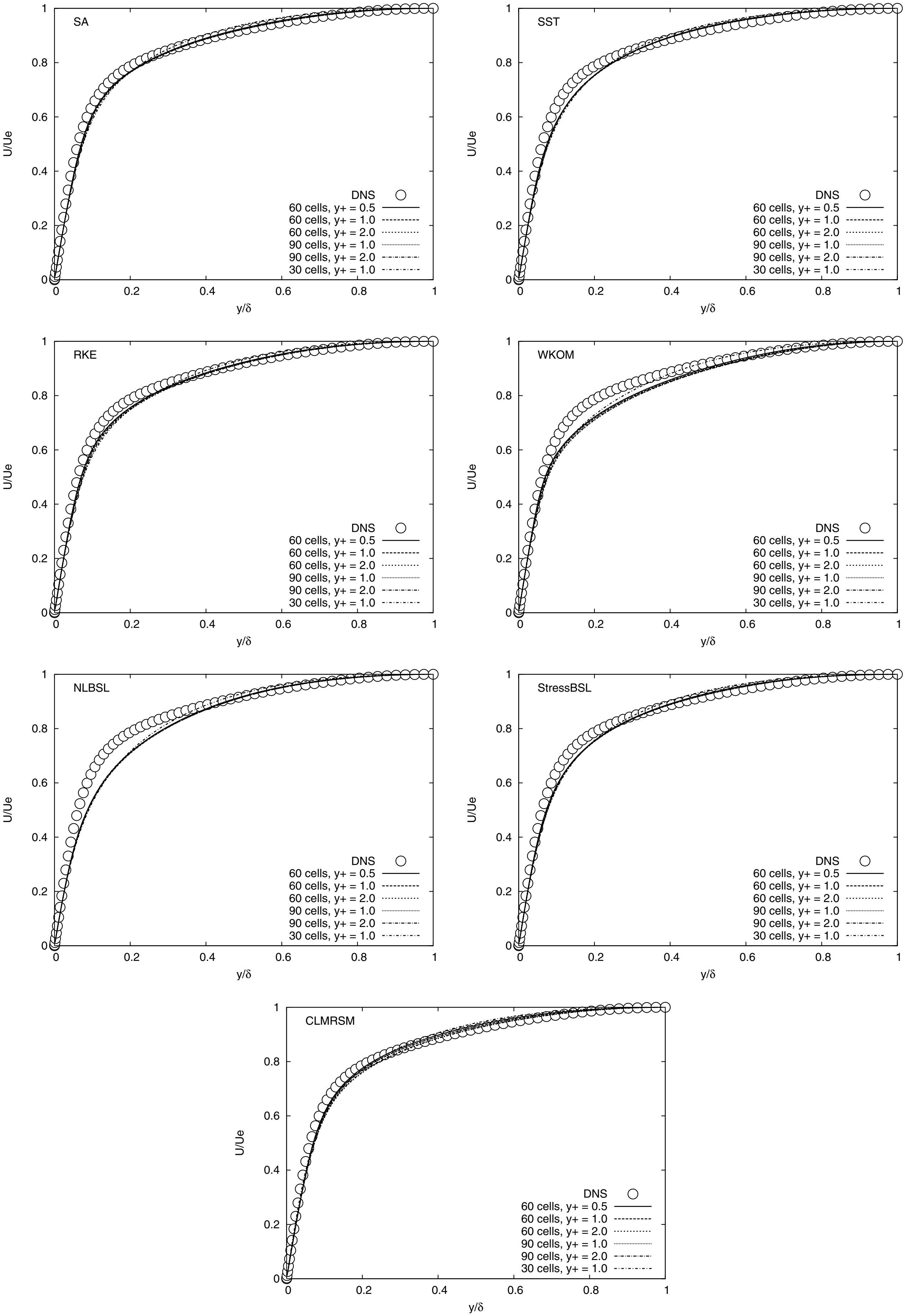

Fig. 5 Channel flow at $Re_\tau = 180$. Boundary layers for different grids.

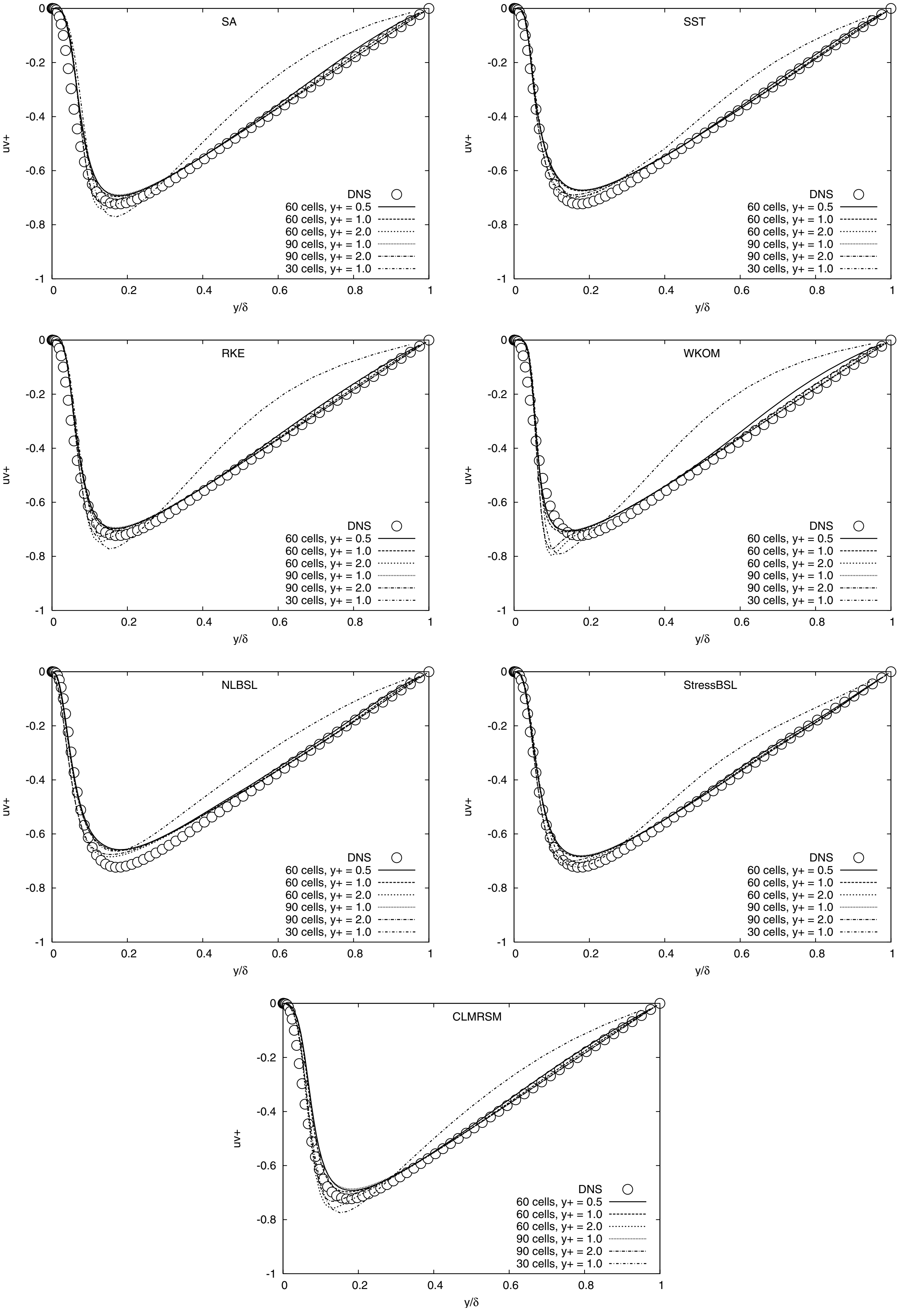

Fig. 6 Channel flow at $Re_\tau = 180$. Shear Reynolds stress for different grids.

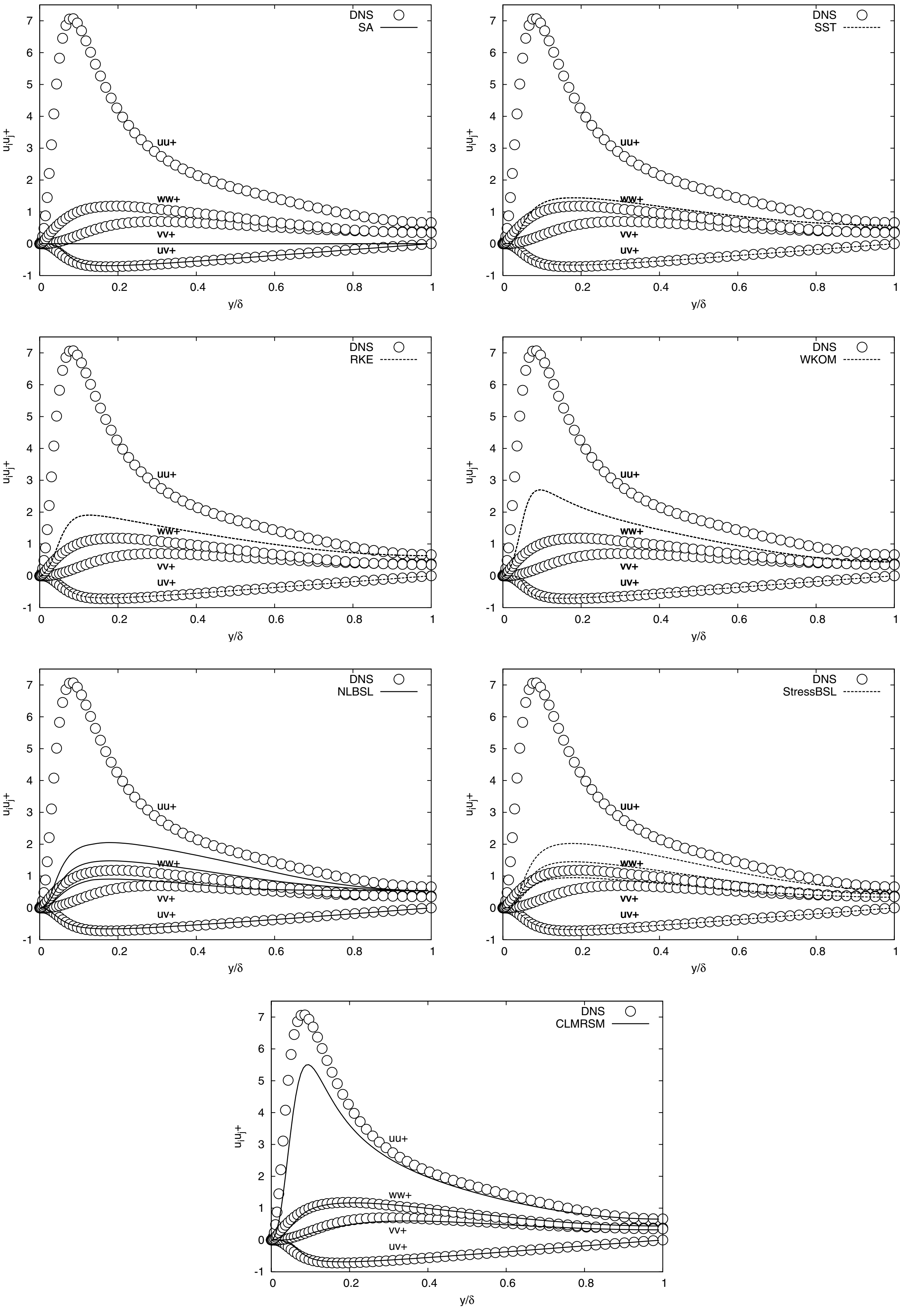

Fig. 7 Channel flow at $Re_\tau = 180$. Present computation and DNS Reynolds stresses.

Additionally, for a selected number of test cases, boundary-layer measurements with an external Pitot probe and laser-Doppler velocimeter (LDV) flow field are also provided. Experimental uncertainty and accuracy levels are provided in [41]. Because of the high quality of the data, these test case and experimental results compose the case A11 of the AGARD-AR-303 report [41], that collects a selection of experimental test cases for the purpose of CFD code validation.

In the present work, an evaluation of mesh refinement effects in the numerical results is initially performed. The resulting best cost-effective mesh is used for the other analyses. Hence, a study of turbulence model effects, at two angles of attack, namely, 1.15 and 2.00 deg, is performed. The lower Reynolds-number condition, with $Re = 3 \times 10^6$, is chosen because the resulting thicker boundary layer may be more largely influenced by the shock wave, being a more demanding test case for the turbulence models. Numerical and experimental pressure distributions are compared for both angles of attack. LDV velocity profile at $x/c = 28\%$ and external-probe boundary layer at $x/c = 95\%$ for the 1.15 deg case are also compared with the respective numerical results. Afterwards transonic polar curves for $Re = 6 \times 10^6$ obtained with selected turbulence models are compared with the T2 and S3MA wind-tunnel results. It is observed that anisotropy is crucial for better turbulence-closure resolution of the complex boundary-layer shock-wave phenomenon. For all simulations, freestream turbulence data according to wind-tunnel data are set as $k_\infty = 0.07$ and $\epsilon_\infty = 0.4$.

2. *Preliminary Mesh-Dependency Evaluation*

A preliminary mesh-dependency evaluation for this test case is performed. The authors remark that this is not a complete mesh-dependency study, but rather an evaluation and confirmation of the used mesh construction directives. The initial mesh is already constructed with knowledge-based qualities, considering all conclusions for mesh configuration described in the current work and also those obtained during the development of the present code. Six mesh configurations, described in Table 1, are considered. Variations in the far-field distance, and overall mesh refinement, are presented in this table. All meshes are designed to provide $y^+ \approx 1$ for the first point away from the wall. For meshes GRID 1, GRID 2, GRID 3, and GRID 6, the far-field distance is varied while overall mesh refinement is kept. Furthermore, successive mesh refinements are obtained with group GRID 1, GRID 4, and GRID 5. Flight conditions are $M_\infty = 0.724$, $Re = 3 \times 10^6$, and $\alpha = 1.15$ deg.

It is interesting to remark here that for the far-field distance variation, exactly the same grid configuration of GRID 1 is used for all other meshes. The extension to the different far-field position in those cases is simply obtained by adding or removing points from the baseline grid, as shown in Fig. 8. This methodology avoids other mesh-dependent solver differences because exactly the same mesh spacing closer to wall is used. A similar approach is directed toward the construction of the refined grids. The mesh GRID 1 is used but with the number of points in all directions multiplied by a factor.

Comparisons of mesh results are made in terms of Cp distributions over the airfoil surface, boundary layer, and shear Reynolds-stress profiles at 60% of the chord, and integrated lift and drag force coefficients. Convergence is considered when the maximum residue of the density field drops 7 orders of magnitude. Lift and drag force coefficients are also monitored. In this mesh-dependency evaluation effort, not all turbulence models are involved, for the sake of computational resource savings. The one-equation SA model is currently chosen for simulations with all meshes in Table 1. It is fairly expected that the conclusions drawn from these models are extensible to the other available models as well.

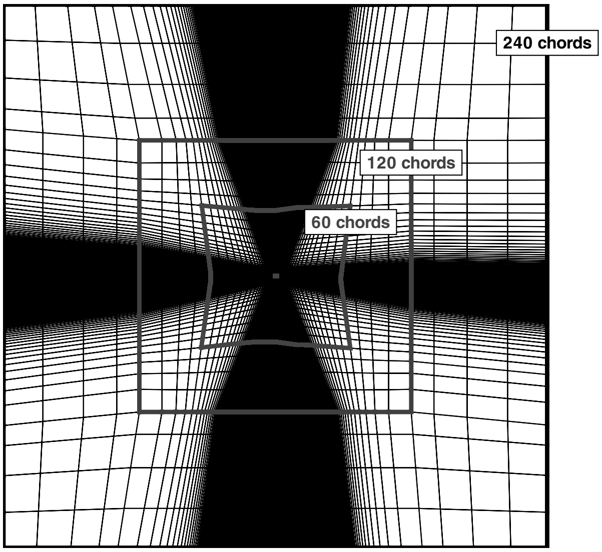

Fig. 8 Sketch of far-field position variation from the baseline grid configuration.

Numerical results for the grids in Table 1 are presented in Fig. 9. It can be observed in this figure that GRID 3, with the far-field region located at 240 chords away from the airfoil, already presents a far-field distance-independent state. Regarding the dependency with the mesh refinement, although solutions present slight variations, the shock-wave position in the longitudinal direction is the same for all meshes. Furthermore almost no dependency with the mesh refinement can be observed in the boundary-layer profiles. Larger but still negligible variation with the mesh refinement is found for the shear stress profiles.

In Tables 2 and 3, a summary of integrated force variation with mesh parameters is presented. The forces are written in terms of the lift and drag force coefficients. The convergence of integrated forces with the increase in the far-field distance can be clearly observed in Table 2. The GRID 3 setting already achieves far-field distance-independent results. In the case of the consecutive mesh refinements in Table 3, the lift coefficient presents slight variations around an average value. The authors attribute the difference of 0.001 from GRID 4 to GRID 5 to cumulative imprecision in the force integration procedure. The drag coefficient presents a clear tendency to converge

Table 2 Lift and drag coefficient variation with mesh parameters: far-field variation

Grid index	Far-field distance	C_l	C_d, counts
GRID 2	60	0.693	135
GRID 1	120	0.698	133
GRID 3	240	0.701	132
GRID 6	320	0.701	132

Table 1 Description of grids over OAT15A airfoil used for mesh-dependency study. All meshes are designed for $y^+ \approx 1$

Grid index	Surface cells	Normal direction cells	Boundary-layer cells	Far-field distance, chords
GRID 1	410	89	34	120
GRID 2	410	85	34	60
GRID 3	410	94	34	240
GRID 6	410	96	34	320
GRID 4	682	135	58	120
GRID 5	822	165	70	120

Table 3 Lift and drag coefficient variation with mesh parameters: refinement variation

Grid index	Surface cells	Boundary-layer cells	C_l	C_d, counts	Relative convergence time
GRID 1	410	34	0.698	133	Reference
GRID 4	682	58	0.701	129	6×
GRID 5	822	70	0.700	128	10×

for more refined grid settings than those of GRID 5. A difference of five counts is observed between the coarser and the finer mesh, which represents a slight variation of 4% in percentage terms. In terms of wall clock time to convergence, GRID 4 takes six times that of reference GRID 1, and GRID 5, ten times that.

From the current observations, there are good indications that the mesh configurations of GRID 3 are fairly acceptable for transonic flow simulations over the OAT15A airfoil. Its configuration represents a cost-effective compromise between adequate numerical solution and reasonable computational resource usage. This conclusion is reinforced when the computational resources used by meshes GRID 3, GRID 4, and GRID 5 are compared. In the OAT15A airfoil simulations to come, the settings of GRID 3 are, thus, employed.

3. *Turbulence Model Comparison*

OAT15A airfoil simulations at $M_\infty = 0.724$, $Re = 3 \times 10^6$, and angles of attack $\alpha = 1.15$ and 2.00 deg are performed. All turbulence models discussed here are compared for such flow cases. As already mentioned, these conditions are chosen because the resulting thicker boundary layer may have a greater interaction with the shock wave, being a more demanding test case for the turbulence models. The third grid configuration in Table 1 is used for the present cases. Convergence is considered when the maximum residue of the density field drops 7 orders of magnitude. However lift and drag coefficients are also monitored to verify force convergence in case density residue would stall.

Numerical pressure coefficient distributions for the $\alpha = 1.15$ deg case obtained with all turbulence models are compared with the respective experimental data, case 14 in AGARD 303 data [41], in Fig. 10. It can be clearly seen in this figure the beneficial effects of anisotropy-capable formulation in the turbulence model. All anisotropy-resolving closures, namely NLBSL, StressBSL, and CLMRSM, present good correlation with the experimental result in capturing the shock-wave position and the overall pressure distribution. As usual with Boussinesq-based eddy-viscosity models, however, all other linear models indicate a further downstream shock-wave location. In the SST case, nevertheless, the eddy-viscosity coefficient, limited by the Bradshaw-type constraint, returns a more feasible result among other linear models.

Similar conclusions are also found for $\alpha = 2.00$ deg results, case 12 in AGARD 303 data [41], in Fig. 11. It is interesting to note that this higher angle of attack represents a more demanding flow condition for the simulations because of the expected stronger shock wave. Besides that, the shock wave is also positioned farther downstream, and it consequently interacts with a thicker boundary layer. In this case, slight differences among the anisotropy-resolving models can be observed. The NLBSL model presents a good representation of the shock-wave solution, whereas CLMRSM unusually computes it slightly upstream and StressBSL, slightly downstream. It is interesting to note that, on the contrary as usual with eddy-viscosity models, which characteristic of overpredicting turbulence levels and returning further downstream shock waves has already been discussed, the more complex CLMRSM closure is capable of computing the shock wave upstream that of the experimental case.

Further comparisons for other flow quantities are also made for $\alpha = 1.15$ deg. As already mentioned, LDV velocity profile at $x/c = 28\%$ and external-probe boundary layer at $x/c = 95\%$ for this case are available. Numerical results are compared with the respective experimental data in Figs. 12 and 13. In Fig. 12, the velocity profiles are made dimensionless referencing the freestream velocity, whereas the outer boundary-layer velocity is used Fig. 13. It is interesting to observe in Fig. 12 that the higher turbulence levels in the linear closures allow for more accelerated flows as a result of the more turbulent and, therefore, more accelerated boundary layers. The NLBSL model presents a striking adherence to the experimental results in the outer velocity profile. Although the StressBSL result initially seems good as well, it overpredicts the boundary-layer thickness, represented by the bend in the numerical velocity profile at about $y/c \approx 0.08$ in Fig. 12. More determining differences are observed in the boundary-layer plots in Fig. 13. A striking match of the boundary layer obtained with NLBSL and the experimental result is seen initially. In this case, no other model achieves such a high accuracy level. SST and CLMRSM adequately compare to the experimental data, whereas other models present more differences. The thicker boundary layer found for StressBSL is also confirmed in Fig. 13. This model presents a rather inconsistent boundary-layer result, with overaccelerated viscous and buffer regions, and much thicker inertial layer.

As an overall conclusion from the present assessment, the advantages in the aerodynamics analyses are clearly seen when anisotropy is considered within the turbulence model formulation for shock-wave boundary-layer interaction. The low- or high-Reynolds number closure formulation does not seem to be determinant in these cases. The NLBSL model presents a considerable advantage over the other currently considered options because it returns much more highly accurate results than the SST model at a similar computational resource usage basis, for the current cases. CLMRSM also presented consistent numerical results.

4. *Polar Curves for OAT15A Airfoil*

In a practical airfoil evaluation from an engineering standpoint, one is interested in the behavior of the airfoil not simply at a single operational condition, but also at off-design conditions. Therefore curves such as lift and drag variation with the angle of attack, as well as the polar curve, are evaluated. The SST, NLBSL, StressBSL, and CLMRSM models are used to estimate such data for the OAT15A airfoil. Flight conditions are $M_\infty = 0.724$ and $Re = 6 \times 10^6$. The angles of attack are considered to be $\alpha = 0$, 2, 3, and 4 deg. This analysis is an ultimate effort for the assessment of the turbulence models at different flow conditions, including separated flow around the section stall situation, in a practical application context. Figure 14 presents the obtained numerical data from these analyses, compared with the respective experimental results.

In Fig. 14a, it can be observed that all models adequately reproduce the lift slope from 0 to 2 deg, with the anisotropy-resolving models returning closer values to the experimental ones. Larger differences are found near the maximum lift, around $\alpha = 3$ deg. All models fail to predict the experimental behavior for angles of attack larger than 2 deg. For SST, NLBSL, and CLMRSM, nonlinear variation of C_l is found for $\alpha > 2$ deg, whereas the experimental data show that the lift still linearly varies with the angle of attack up to $\alpha = 3$ deg. NLBSL shows the more abrupt lift loss at $\alpha = 3$ deg. Although StressBSL returns linear variation of the lift up to $\alpha = 3$ deg, it misses the stall as the lift still increases up to $\alpha = 4$ deg. Although SST and CLMRSM miss the maximum lift at $\alpha = 3$ deg, they interestingly returns good values of lift at the off-design $\alpha = 4$ deg condition, which already contains considerable separated flow regions.

The drag results in Fig. 14b indicate that SST and CLMRSM are closer to the experimental data than NLBSL and StressBSL. The unexpected boundary-layer behavior found for the StressBSL model in Fig. 13 explains the much higher drag values found for this model

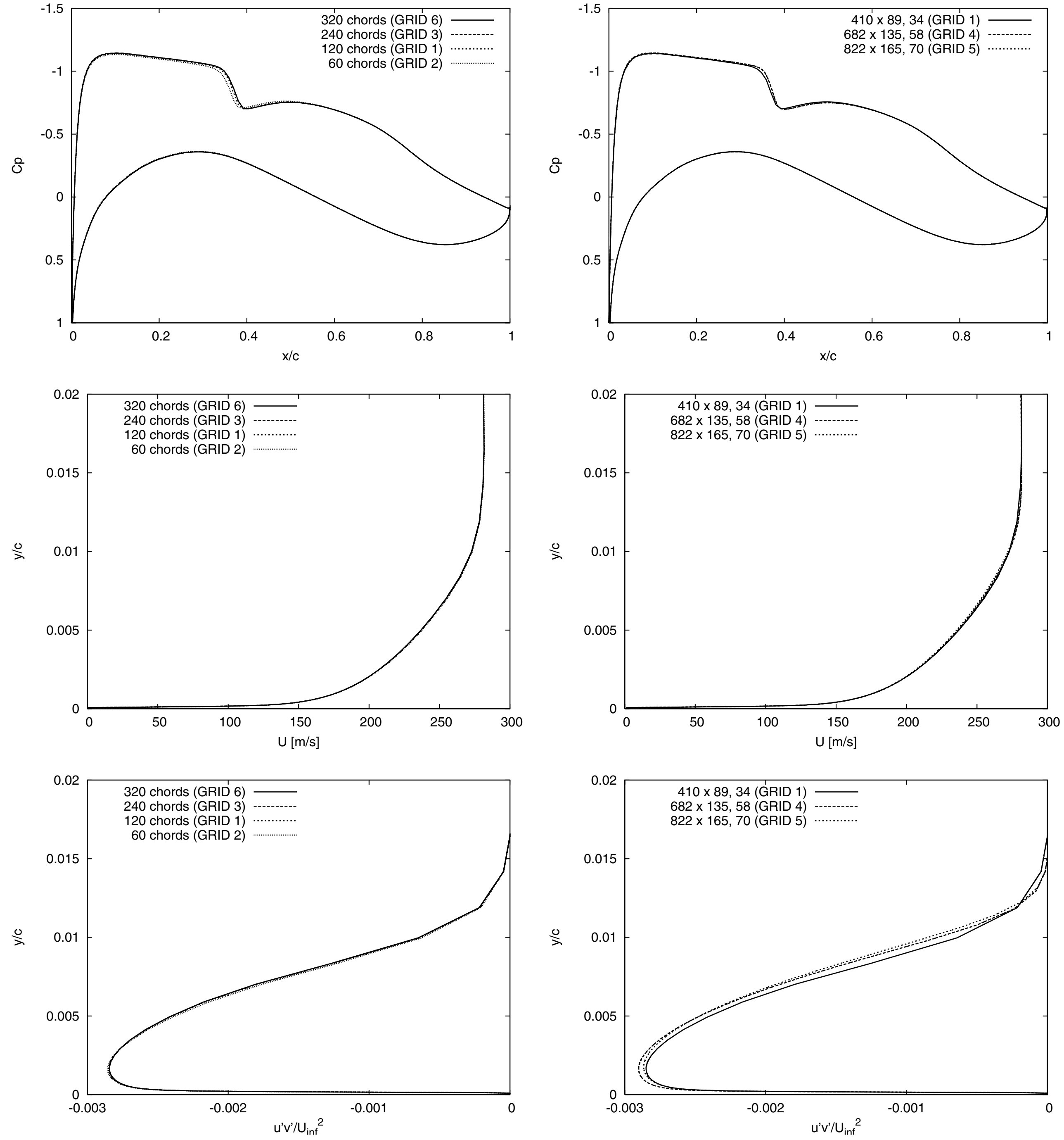

a) Farfield variation **b) Refinement variation**

Fig. 9 ***Cp*, boundary layer, and shear Reynolds-stress profiles for different mesh configurations.**

in Fig. 14b. As a consequence of the lower lift values computed by NLBSL for $\alpha > 2$ deg in Fig. 14a, the drag results are also lower than the experimental ones. Except at $\alpha > 2$ deg, SST and CLMRSM predict reasonable drag values when compared with the experimental data, with CLMRSM predicting slightly larger values than SST. At $\alpha = 2$ deg, numerical values are considerably larger than the experimental results.

In Figs. 14c and 14d, one can find these data plotted in terms of practical engineering results that are usually considered when designing and choosing an airfoil. In Fig. 14c, the lift-to-drag ratio is plotted against the angle of attack, whereas the drag polar is found in Fig. 14d. It is interesting to observe that all models fail to predict the high lift-to-drag ratio observed around $\alpha = 2$ deg, which is close to the already mentioned design point of this airfoil. For the other angles of attack, however, all models approach the experimental data, with SST and CLMRSM presenting very close results to the wind tunnel ones. In Fig. 14d, the polar drag curve is presented. One conclusion from the curves in this plot is that in general, for the a given lift coefficient, the models overpredict the drag coefficient values. From an engineering point of view, this is not the optimum situation, but it is not that bad because the larger drag values are at least a conservative approach for a design stage.

VI. Conclusions

The paper presents results obtained with a finite-volume code developed to solve the compressible RANS equations. Turbulence effects are included by several advanced turbulence models, which are specifically designed for aerospace-type flows. The options here range from linear to nonlinear eddy-viscosity models, as well as

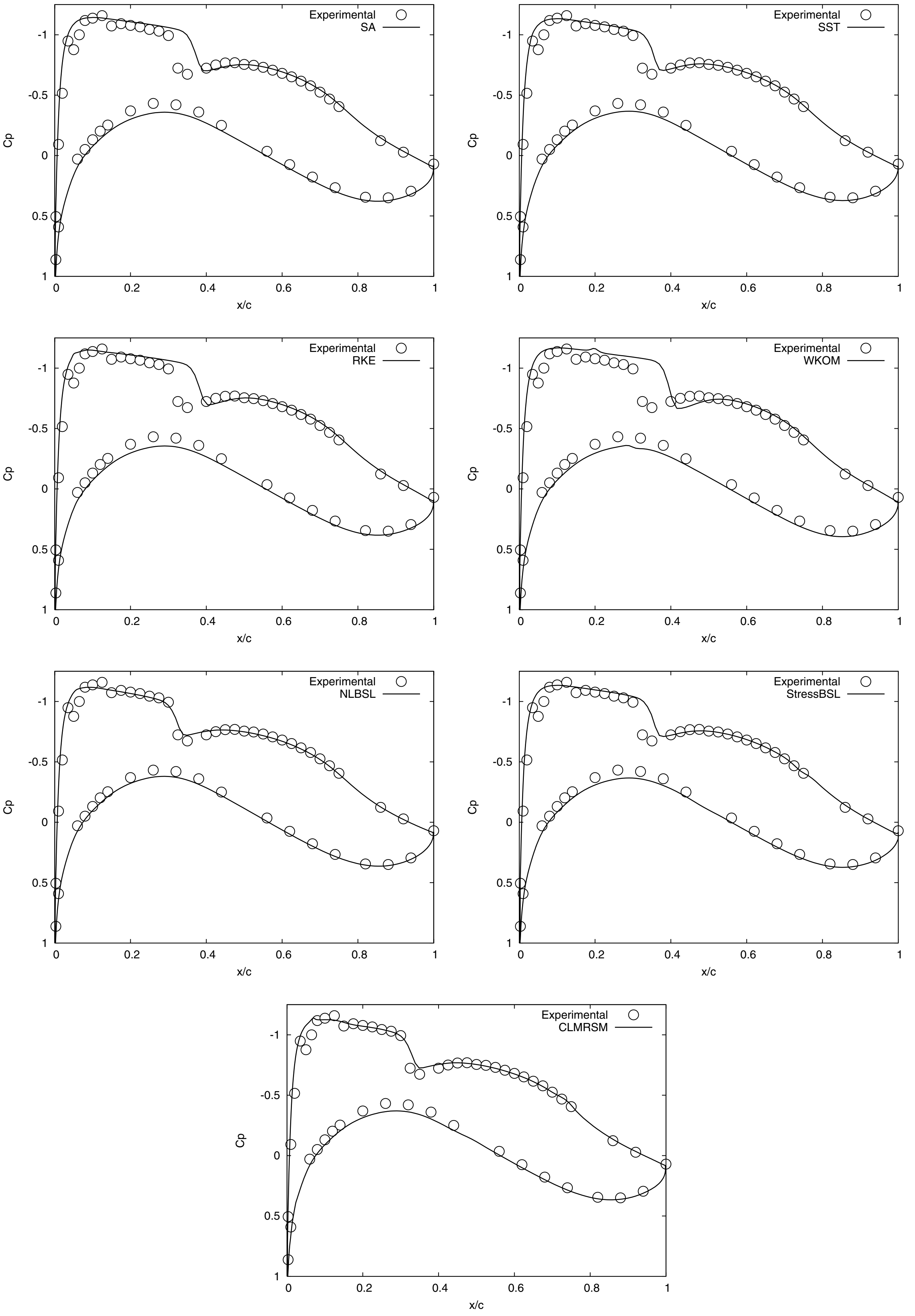

Fig. 10 Numerical and experimental *Cp* distributions for flow conditions $M_\infty = 0.724$, $Re = 3 \times 10^6$, and $\alpha = 1.15$ deg.

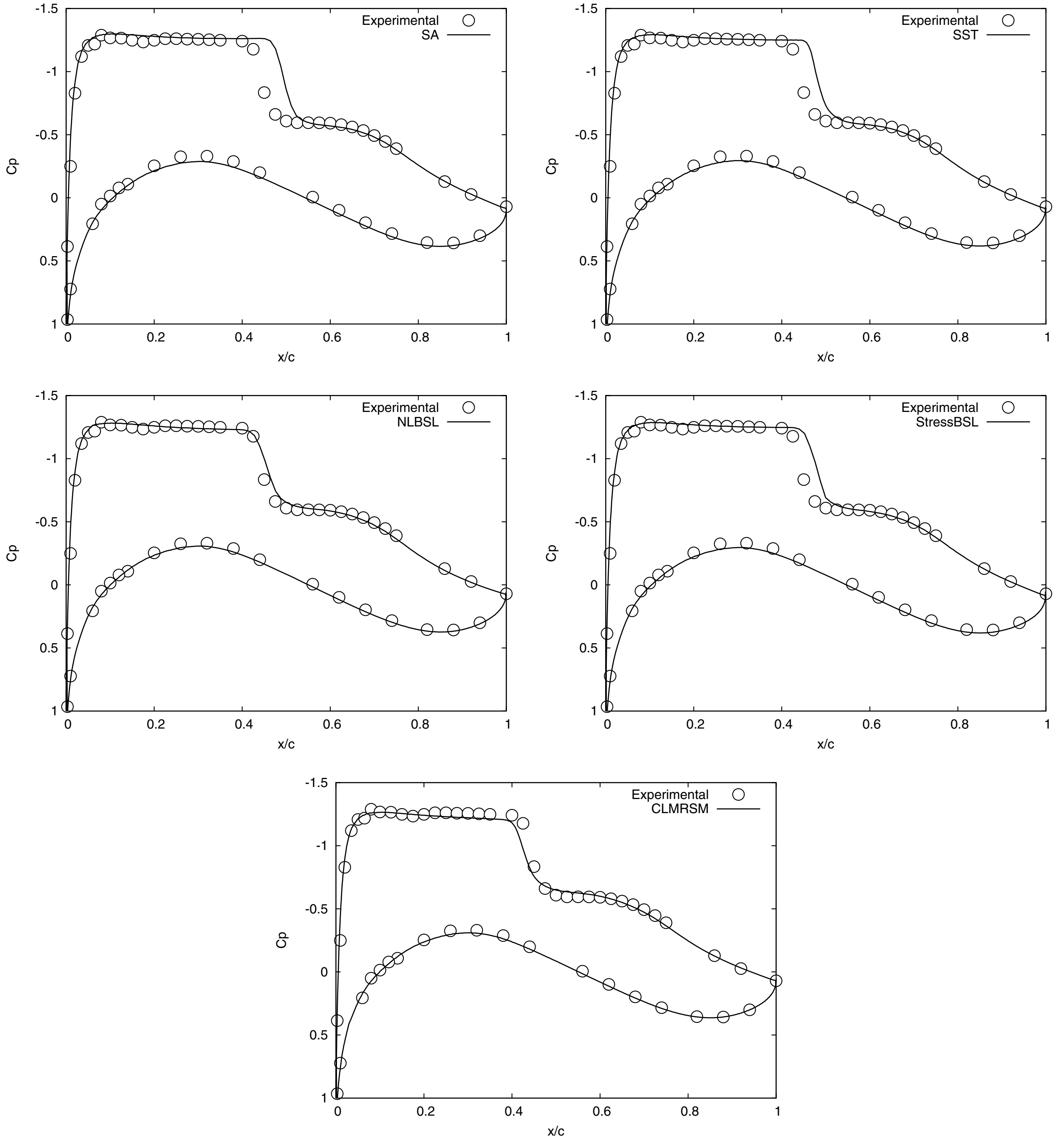

Fig. 11 Numerical and experimental *Cp* distributions for flow conditions $M_\infty = 0.724$, $Re = 3 \times 10^6$, and $\alpha = 2.00$ deg.

Reynolds-stress closures. An explicit algebraic expansion of a simplified Reynolds-stress equation is used to compose the nonlinear model.

Validation against wind-tunnel and DNS data for flat-plate and parallel-wall channel flow cases shows the levels of turbulence representativeness that is obtained with each modeling approach. Mesh-dependency studies show that all presently considered models are similar in terms of mesh configuration requirements. It is observed that all models adequately return mean flow and turbulence parameters when compared with the reference data. However differences can be observed when anisotropy is considered within the model formulation. In these cases, separation of normal stresses can be observed.

Transonic flow simulations about a supercritical airfoil indicate that the anisotropy of the normal stresses is of paramount importance for the successful computation of shock-wave/boundary-layer flows. However although anisotropy-resolving closures indeed return more consistent results, it is observed that they still fail to predict the expected divergence onset due to strong shock-wave boundary-layer interaction in this case. Effects such as early stall or higher drag values at lower angles of attack are observed. In general, however, the more advanced models still outperform the linear closures, except for the SST model, which yields results close to those obtained with the nonlinear and Reynolds-stress models, at least in terms of integrated coefficients.

It is interesting to point out that the NLBSL model presents results close to, or even better than those obtained with the Reynolds-stress closures exercised here. Its computational cost, however, is as low as that of a standard two-equation model. Therefore in terms of overall performance, this model presents the best cost-effect compromise for the transonic airfoil case. Hence additional effort on recalibrating and extending this model to cope with the limitations indicated in the

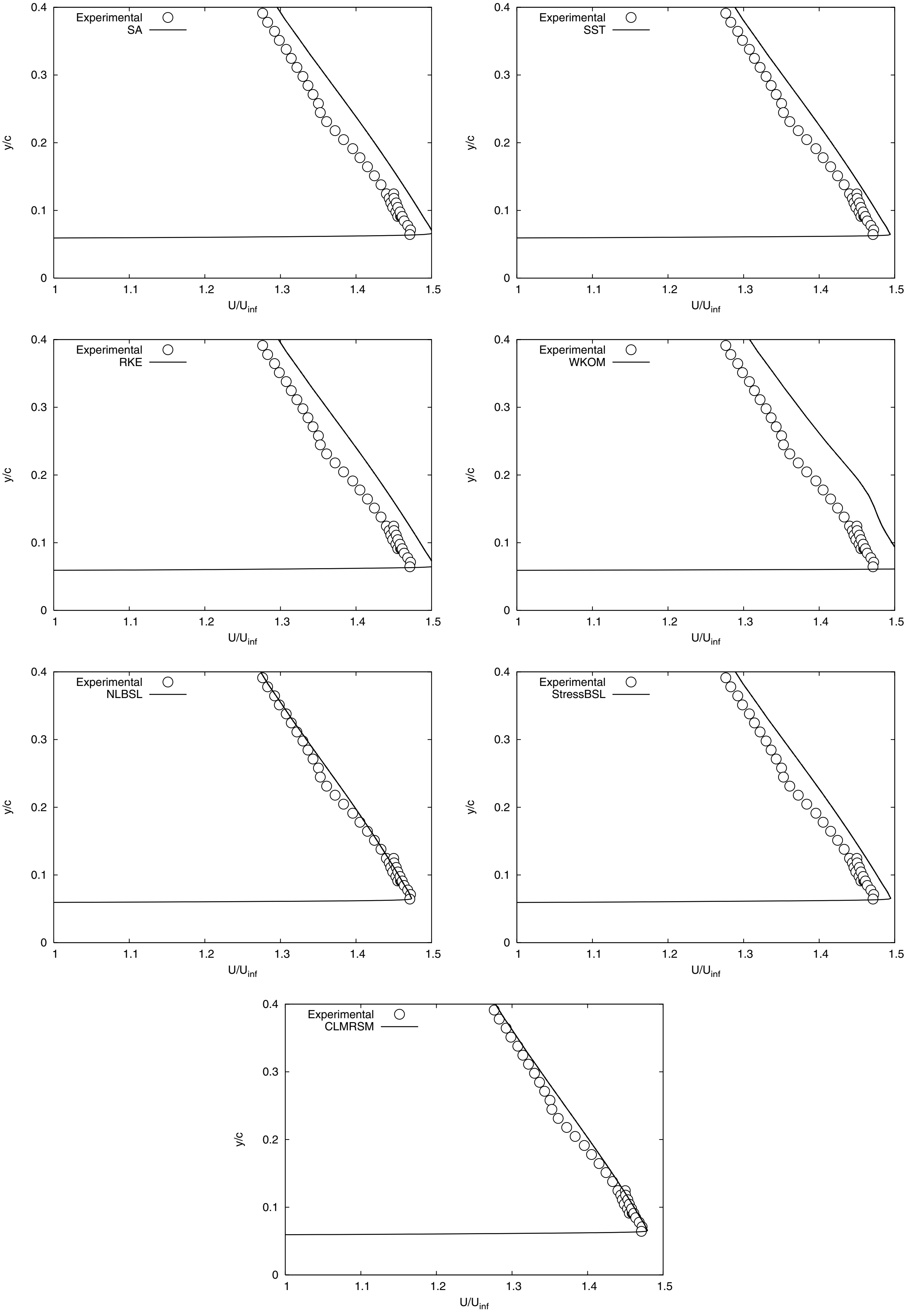

Fig. 12 Numerical and experimental velocity profiles at $x/c = 28\%$ for flow conditions $M_\infty = 0.724$, $Re = 3 \times 10^6$, and $\alpha = 1.15$ deg.

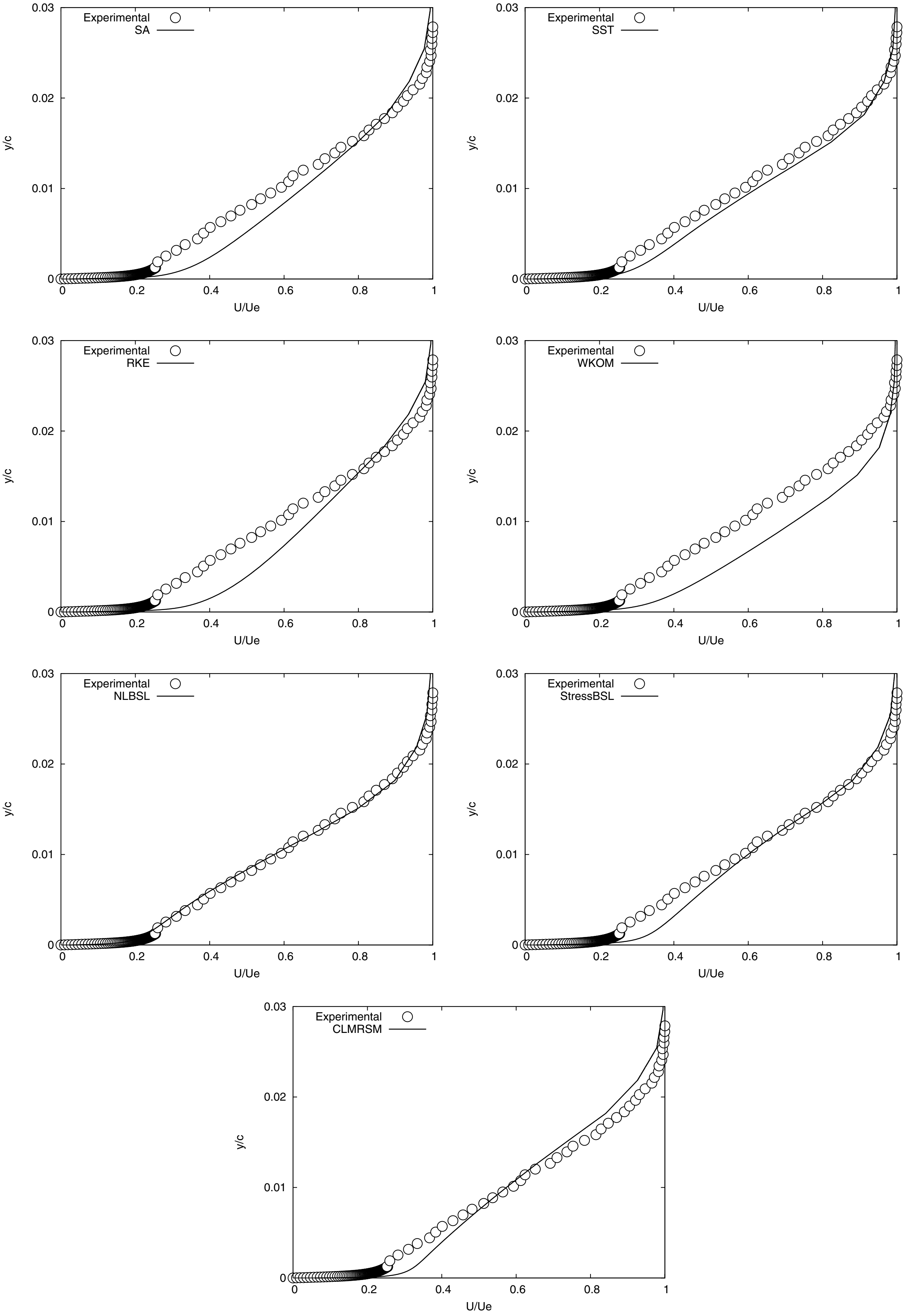

Fig. 13 **Numerical and experimental boundary layers at $x/c = 95\%$ for flow conditions $M_\infty = 0.724$, $Re = 3 \times 10^6$, and $\alpha = 1.15$ deg.**

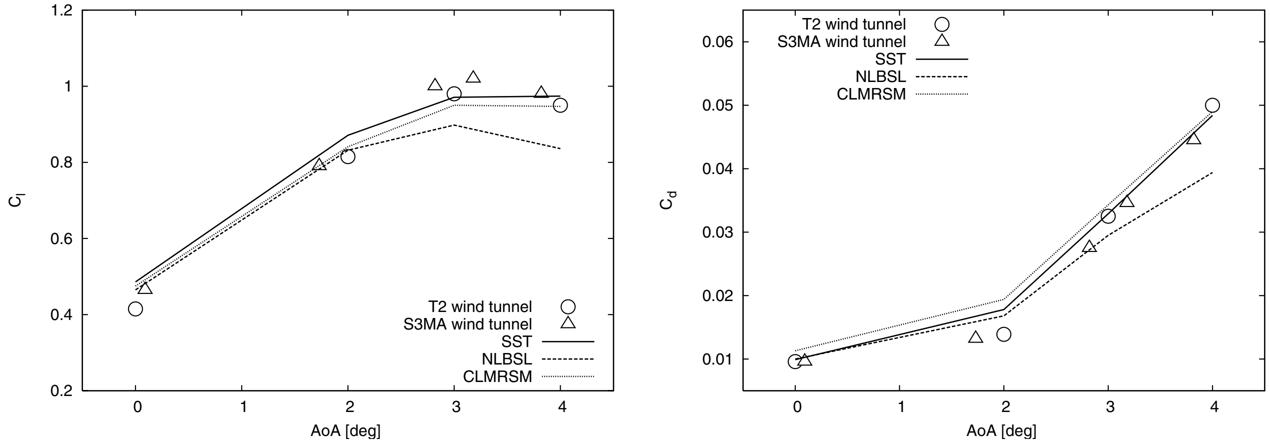

a) Lift **b) Drag**

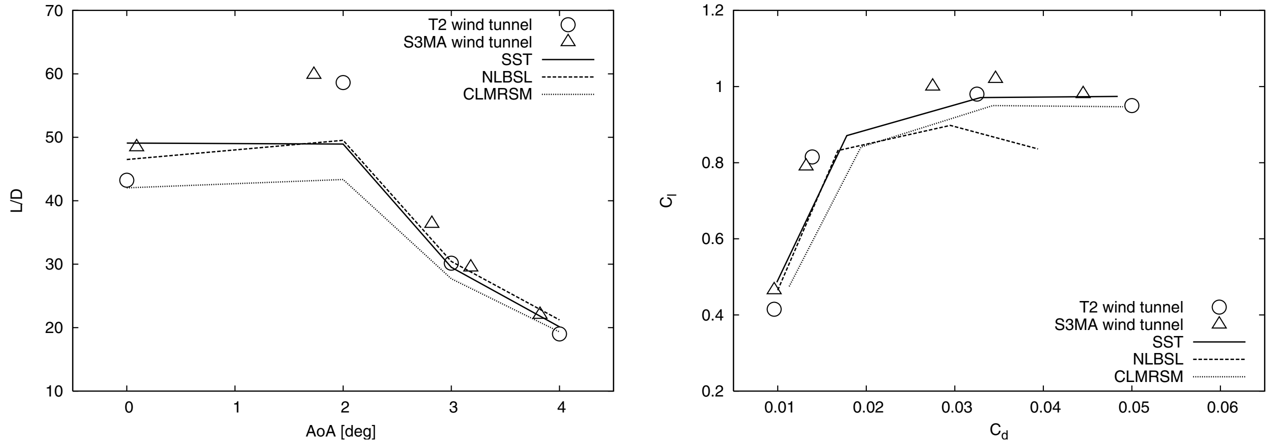

c) Lift to drag **d) Polar**

Fig. 14 Numerical and experimental force coefficient results for flow conditions $M_\infty = 0.724$ and $Re = 6 \times 10^6$.

current work is clearly a good investment. Furthermore the models currently implemented in the code and the experience acquired in the present study have advanced the capability of simulating the transonic and supersonic flows of interest to IAE, which motivated the current effort.

Acknowledgments

The authors would like to acknowledge Conselho Nacional de Desenvolvimento Científico e Tecnológico (CNPq), which partially supported the project under the Integrated Project Research Grant No. 501200/2003-7. The authors also acknowledge P. Batten at Metacomp Technologies, Inc., and S. Wallin at Linköping University, Sweden, for their insight on the specifics of the respective turbulence model implementations.

References

[1] Bigarella, E. D. V., Basso, E., and Azevedo, J. L. F., "Centered and Upwind Multigrid Turbulent Flow Simulations with Applications to Launch Vehicles," AIAA Paper 2004-5384, Aug. 2004.

[2] Spalart, P. R., and Allmaras, S. R., "A One-Equation Turbulence Model for Aerodynamic Flow," *La Recherche Aeropastiale*, Vol. 1, Jan.–Feb. 1994, pp. 5–21.

[3] Menter, F. R., "Zonal Two Equation *k–ω* Turbulence Models for Aerodynamic Flows," AIAA Paper 93-2906, July 1993.

[4] Bigarella, E. D. V., "Three-Dimensional Turbulent Flow Simulations over Aerospace Congurations," M.Sc. Thesis, Instituto Tecnológico de Aeronáutica, São José dos Campos, SP, Brazil, Dec. 2002.

[5] Carlson, J. R., "Applications of Algebraic Reynolds Stress Turbulence Models, Part 2: Transonic Shock-Separated Afterbody," *Journal of Propulsion and Power*, Vol. 13, No. 5, 1997, pp. 620–628.

[6] Rizzetta, D. P., "Evaluation of Explicit Algebraic Reynolds-Stress Models for Separated Supersonic Flows," *AIAA Journal*, Vol. 36, No. 1, 1998, pp. 24–30.

[7] Lien, F. S., Kalitzin, G., and Durbin, P. A., "RANS Modeling for Compressible and Transitional Flows," *Proceedings of the 1998 Summer Program: Center for Turbulence Research*, Stanford Univ., Stanford, CA, 1998.

[8] Batten, P., Craft, T. J., Leschziner, M. A., and Loyau, H., "Reynolds-Stress-Transport Modeling for Compressible Aerodynamics Applications," *AIAA Journal*, Vol. 37, No. 7, 1999, pp. 785–796.

[9] Leschziner, M. A., and Loyau, H., "Numerical Investigation of Three-Dimensional Transonic Flow with Large Separation," *Proceedings of the 22nd International Congress of Aeronautical Sciences*, International Council of Aeronautical Sciences Paper 262, 2000.

[10] Leschziner, M. A., Batten, P., and Loyau, H., "Modelling Shock-Affected Near-Wall Flows with Anisotropy-Resolving Turbulence Closures," *International Journal of Heat and Fluid Flow*, Vol. 21, No. 3, June 2000, pp. 239–251.

[11] Leschziner, M. A., and Drikakis, D., "Turbulence Modelling and Turbulent-Flow Computation in Aeronautics," *The Aeronautical Journal*, Vol. 106, No. 1061, July 2002, pp. 349–383.

[12] Gerolymos, G. A., Sauret, E., and Vallet, I., "Oblique-Shock-Wave/Boundary-Layer Interaction Using Near-Wall Reynolds-Stress Models," *AIAA Journal*, Vol. 42, No. 6, 2004, pp. 1089–1100.

[13] Shih, T., Liou, W. W., Shabbir, A., Yang, Z., and Zhu, J., "A New Eddy Viscosity Model for High Reynolds Number Turbulent Flows: Development and Validation," NASA TM 106721, NASA Lewis Research Center, Cleveland, OH, Aug. 1994.

[14] Anon., *FIDAP 8: Tutorial Manual*, Fluent, Inc., Lebanon, NH, 1998.

[15] Wallin, S., and Johansson, A. V., "An Explicit Algebraic Reynolds Stress Model for Incompressible and Compressible Turbulent Flows," *Journal of Fluid Mechanics*, Vol. 403, Jan. 2000, pp. 89–132.

[16] Hellsten, A., "New Advanced *k–ω* Turbulence Model for High-Lift Aerodynamics," *AIAA Journal*, Vol. 43, No. 9, Sept. 2005, pp. 1857–1869.

[17] Scalabrin, L. C., "Numerical Simulation of Three-Dimensional Flows over Aerospace Congurations," M.Sc. Thesis, Instituto Tecnológico de Aeronáutica, São José dos Campos, SP, Brazil, July 2002.

[18] Bigarella, E. D. V., and Azevedo, J. L. F., "A Study of Convective Flux Computation Schemes for Aerodynamic Flows," AIAA Paper 2005-0633, Jan. 2005.

[19] Anderson, J. D., Jr., *Fundamentals of Aerodynamics*, 2nd ed., McGraw–Hill, New York, 1991, Chap. 15, p. 647.

[20] Roe, P. L., "Approximate Riemann Solvers, Parameter Vectors, and Difference Schemes," *Journal of Computational Physics*, Vol. 43, No. 2, Oct. 1981, pp. 357–372.

[21] Van Leer, B., "Towards the Ultimate Conservative Difference Scheme, V: A Second-Order Sequel to Godunov's Method," *Journal of Computational Physics*, Vol. 32, No. 1, July 1979, pp. 101–136.

[22] Barth, T. J., and Jespersen, D. C., "The Design and Application of Upwind Schemes on Unstructured Meshes," AIAA Paper 89-0366, 1989.

[23] Spalart, P. R., "Strategies for Turbulence Modelling and Simulations," *International Journal of Heat and Fluid Flow*, Vol. 21, No. 3, 2000, pp. 252–263.

[24] Menter, F. R., "Two-Equation Eddy-Viscosity Turbulence Models for Engineering Applications," *AIAA Journal*, Vol. 32, No. 8, 1994, pp. 1598–1605.

[25] Wilcox, D. C., *Turbulence Modeling for CFD*, 2nd ed., DCW Industries, La Cañada, CA, 1998.

[26] Jones, W. P., and Launder, B. E., "The Prediction of Laminarization with a Two-Equation Model of Turbulence," *International Journal of Heat and Mass Transfer*, Vol. 15, No. 2, 1972, pp. 301–314.

[27] Johnson, D. A., and King, L. S., "A Mathematically Simple Turbulence Closure Model for Attached and Separated Turbulent Boundary Layers," *AIAA Journal*, Vol. 23, No. 11, Nov. 1985, pp. 1684–1692.

[28] Craft, T. J., and Launder, B. E., "A Reynolds Stress Closure for Complex Geometries," *International Journal of Heat and Fluid Flow*, Vol. 17, No. 3, 1996, pp. 245–254.

[29] Lumley, J. L., "Computational Modeling of Turbulent Flows," *Advances in Applied Mechanics*, edited by C.-S. Yih, Vol. 18, Academic Press, New York, 1978, pp. 123–176.

[30] Daly, B., and Harlow, F., "Transport Equation in Turbulence," *Physics of Fluids*, Vol. 13, 1970, pp. 2634–2649.

[31] Rotta, J., "Statistischer Theorie Nichthomogener Turbulenz 1," *Zeitschrift für Physik*, Vol. 129, No. 6, 1951, pp. 547–572.

[32] Launder, B. E., Reece, G. J., and Rodi, W., "Progress in the Development of a Reynolds-Stress Turbulence Closure," *Journal of Fluid Mechanics*, Vol. 68, No. 3, 1975, pp. 537–566.

[33] Craft, T. J., Launder, B. E., and Suga, K., "Development and Application of a Cubic Eddy-Viscosity Model of Turbulence," *International Journal of Heat and Fluid Flow*, Vol. 17, No. 2, 1996, pp. 108–115.

[34] Hellsten, A., "New Two-Equation Turbulence Model for Aerodynamics Applications," Ph.D. thesis, Helsinki Univ. of Technology, Laboratory of Aerodynamics, Finland, Jan. 2004.

[35] Tennekes, H., and Lumley, J. L., *A First Course in Turbulence*, MIT Press, Cambridge, MA, 1972.

[36] Klebano, P. S., "Characteristics of Turbulence in a Boundary Layer with Zero Pressure Gradient," NACA TR-1247, National Bureau of Standards, Washington, D.C., 1955.

[37] Coles, D. E., and Hirst, E. A., "Computation of Turbulent Boundary Layers," *Proceedings of the 1968 U.S. Air Force Office of Scientific Research–Internal Flow Program: Stanford Conference*, Vol. 2, Stanford Univ., Palo Alto, CA, 1969.

[38] Swanson, R. C., Radespiel, R., and Turkel, E., "On Some Numerical Dissipation Schemes," *Journal of Computational Physics*, Vol. 147, No. 2, Dec. 1998, pp. 518–544.

[39] Bardina, J. E., Huang, P. G., and Coakley, T. J., "Turbulence Modeling Validation, Testing, and Development," NASA TM-110446, NASA Ames Research Center, Moffett Field, CA, 1997.

[40] Kim, J., Moin, P., and Moser, R., "Turbulence Statistics in Fully Developed Channel Flow at Low Reynolds Number," *Journal of Fluid Mechanics*, Vol. 177, Apr. 1987, pp. 133–166.

[41] Rodde, A. M., and Archambaud, J. P., "OAT15A Airfoil Data," A Selection of Experimental Test Cases for the Validation of CFD Codes, NATO AGARD, No. AGARD-AR-303, Aug. 1994, Case A11.

[42] Archambaud, J. P., and Mignosi, A., "Two-Dimensional and Three-Dimensional Adaptation at the T2 Transonic Wind Tunnel of ONERA/CERT," AIAA Paper 88-2038, May 1988, pp. 342–350.

[43] Grandjacques, M., "S3MA Supersonic Test Capabilities Extension Using Half Nozzles," ONERA TP 1997-56, Aussois, France, May 1997.

P. Givi
Associate Editor